Controlled Neighbor Exchanges Drive Glassy Behavior, Intermittency, and Cell Streaming in Epithelial Tissues

Amit Das[®], Srikanth Sastry[®], and Dapeng Bi[®]

¹Department of Physics, Northeastern University, Boston, Massachusetts 02115, USA ²Jawaharlal Nehru Centre for Advanced Scientific Research, Jakkur Campus, Bangalore 560064, India

(Received 1 May 2020; revised 23 August 2021; accepted 23 September 2021; published 22 November 2021)

Cell neighbor exchanges are integral to tissue rearrangements in biology, including development and repair. Often, these processes occur via topological T1 transitions analogous to those observed in foams, grains, and colloids. However, in contrast to those in nonliving materials, the T1 transitions in biological tissues are rate limited and cannot occur instantaneously due to the finite time required to remodel complex structures at cell-cell junctions. Here, we study how this rate-limiting process affects the mechanics and collective behavior of cells in a tissue by introducing this important biological constraint in a theoretical vertex-based model as an intrinsic single-cell property. We report that, in the absence of this time constraint, the tissue undergoes a glass transition with lowering of cell motility characterized by a sharp increase in the intermittency of cell-cell rearrangements. Remarkably, this glass transition disappears, as T1 transitions are temporally limited. As a unique consequence of limited rearrangements, we also find that the tissue develops spatially correlated populations of fast and slow cells, in which the fast cells organize into streamlike patterns and maintain optimally stable cell-cell contacts. The predictions of this work are compared with existing *in vivo* experiments in *Drosophila* pupal development.

DOI: 10.1103/PhysRevX.11.041037 Subject Areas: Biological Physics, Soft Matter,
Statistical Physics

I. INTRODUCTION

Cell neighbor exchange is fundamental to a host of active biological processes, from embryonic development [1,2] to tissue repair [3,4]. Often referred to as cell intercalations [5,6], it is the leading mode of rearrangement in a confluent cell packing and in the simplest form described by a topological T1 process observed in foams [7]. During development, T1 rearrangements lead to diverse reorganization patterns [8–12], based on polarized global cues [13,14], or apparently random localized active fluctuations [15,16]. Disruption of neighbor exchanges leads to defects in developing embryos [13,14], while an increase is shown to alleviate disease conditions [8,17]. It is, therefore, important that the underlying biological programs of neighbor exchanges are regulated in a tissue.

A common feature that nearly all experiments following cell intercalations point out is that there is always a finite time delay involved with the T1 processes. The most basic form of delay comes from the fact that any T1 event requires a modification of the adherens junctions between

Published by the American Physical Society under the terms of the Creative Commons Attribution 4.0 International license. Further distribution of this work must maintain attribution to the author(s) and the published article's title, journal citation, and DOI. cells which are made of homotypic bonds between E-cadherin receptors across two cells, supported by actomyosin networks and other adhesion molecules like α - and β -catenin. The dynamics in tissues are always highly stochastic and overdamped. There are several dissipative processes, like the friction from the membranes at the contact, actomyosin cortices of the cells involved, other filamentous structures in the cytoskeleton, and cytoplasm of the two cells, that slow down the movement of the adhesion molecules associated with junction remodeling [13,18–26]. Several papers over the past two decades report timescales associated with the dynamics of T1 transitions in converging and extending Drosophila germ band. Bertet and co-workers [13] measure typical timescales of 10 min for junction shrinkage and another 10 min for reextension. The combination of these two timescales introduces a natural time delay between successive T1 events involving a given cell. They also report almost doubling of this time delay in gap gene Krüppel mutant embryos attributed to a defect in the polarization of myosin-II at the anteriorposterior junctions. This means the arrangement of molecules at the junctions can give rise to a time delay which can be modified by perturbations. Blankenship et al. [27] report similar timescales of junction remodeling (approximately 7-8 min for shrinkage and approximately 5-8 min for reelongation). In more recent works, Simões, Mainieri, and Zallen [28] report a rate of one T1 event per cell in 30 min, and Wang *et al.* [29] report a nonmonotonic variation of T1 rate in the range 0–0.1 per cell per minute in *Drosophila* germ band. Curran *et al.* [16] measure T1 rates in *Drosophila* pupal notum, where a monotonic drop in T1 rate is observed during tissue maturation. All these results confirm that not only is there a natural time delay associated with T1 events, this delay can vary during the developmental process or be modified by mutation. Curran *et al.* [16] also show potential ways to tune the natural time delay by perturbation of the Rho-signaling pathway. Based on these examples, it is clear that cellular rearrangements are associated with time delays with origins in the cellular machinery driving the neighbor exchanges based on intra- and extracellular cues and frictional forces from the cell-cell contacts.

While there is a scarcity of quantitative measurement of cell-level neighbor exchange rates [16,28,29], recent evidence suggests that limiting the rate of neighbor exchanges influences many tissue-level properties. The fluidity of an epithelium [30] is affected by differential rates of neighbor exchanges in development [16,31]. Neighbor exchanges and dynamic remodeling of cell-cell contacts [32,33] are crucial in collective cell migration through dense environments; examples include the migration of border cells in developing *Drosophila* oocyte [34], the formation of dorsal branches in *Drosophila* tracheae [35], and the formation of zebrafish posterior lateral line primordium [36]. In in vitro human bronchial epithelial monolayers, T1 rearrangements are required for fluidization, yet isolated T1s are difficult to capture even during unjamming as the cellular collective often fluidizes by forming collective, coherently moving packs [37,38]. Similarly, invading cancer cells often form multicellular streams to migrate through narrow spaces in rigid tissues [39-45] that depend crucially on neighbor exchanges, as suggested recently [46].

Despite this evidence, it is unclear how the dynamics of neighbor exchanges and dynamic remodeling of cell-cell contacts are related and what roles they play in the emergent multicellular behavior. In this work, we try to understand this relation within a theoretical approach. We extend the well-known 2D vertex model [47,48], which has already provided valuable insights on morphogenesis [49,50], epithelial maturation [37], unjamming [38], and wound healing [51]. In all these cases, the T1 events are considered instantaneous [48,52], implicit [53], with an embargo timer [54] or controlled using a Monte Carlo scheme [55]. However, the interactions of single-cell motility and the rate of T1 events have not been considered.

The focus of this work is to study the interplay of active cell motility and the controlled rate of T1 events regulated at the level of individual cells. We explore this relation and its consequences within a theoretical approach by a single-cell temporal control on cellular neighbor exchanges in terms of a characteristic timescale for which T1 transitions are stalled. We use an extended dynamic vertex model to

investigate how this rate constraint influences epithelial tissue properties, both material and functional. A rich set of dynamical regimes emerges as a result of this control. Changing the intrinsic cell-level persistence time for T1 events induces a gradual slowing of the cellular dynamics. Though this is reminiscent of the dynamical arrest in glassy systems, the nature of the glassy state that emerges is distinct and not previously described. The interplay of cell motility and intrinsic persistence of T1 events gives rise to out-of-equilibrium states that behave as a glassy system yet lacks conventional dynamic heterogeneity and, surprisingly, contains a population of mobile cells that can migrate via an unusual coordinated streamlike motion. In addition, the tissue develops collective migration patterns akin to cell streaming in cancerous tissues [41,44]. We also demonstrate that single-cell control yields realistic neighbor exchange rates and correctly captures the relationship observed between the rate of neighbor exchanges and cellular junctional tensions in a developing *Drosophila* pupa [16].

II. DYNAMIC VERTEX MODEL

A. Equations of motion and forces

Our appropriately modified "dynamic vertex model" (DVM) [38] retains most of the classic features [53,56,57]. Cells in a 2D epithelial monolayer are described by irregular polygons [Fig. 1(a)], defined using vertices, which constitute the degrees of freedom for the model. The vertex positions $\{r_i\}$ evolve against a uniform frictional drag ζ according to the overdamped athermal equations of motion

$$\zeta \frac{d\mathbf{r}_i}{dt} = \mathbf{f}_i^{\text{shape}} + \mathbf{f}_i^{\text{active}}.$$
 (1)

The forces $\mathbf{f}_i^{\text{shape}}$ and $\mathbf{f}_i^{\text{active}}$ are described below.

Because of the biomechanical interactions, cells resist changes to their shapes, described by the tissue mechanical energy [48,56,57]

$$E = \sum_{i=1}^{N} \left[K_A (A_i - A_0)^2 + K_P (P_i - P_0)^2 \right], \qquad (2)$$

where N is the number of cells and A_i and P_i are the area and the perimeter of cell i, respectively. A_0 and P_0 are the equilibrium cell area and perimeter, respectively, considered uniform across the tissue [58]. K_A and K_P are the elastic moduli associated with deformations of the area and perimeter, respectively. The second term in the right-hand side of Eq. (2) yields a dimensionless target cell shape index $p_0 = P_0/\sqrt{A_0}$ [37,38]. The force on any vertex due to cell shape fluctuations is

$$\mathbf{f}_{i}^{\text{shape}} = -\frac{\partial E}{\partial \mathbf{r}_{i}}.$$
 (3)

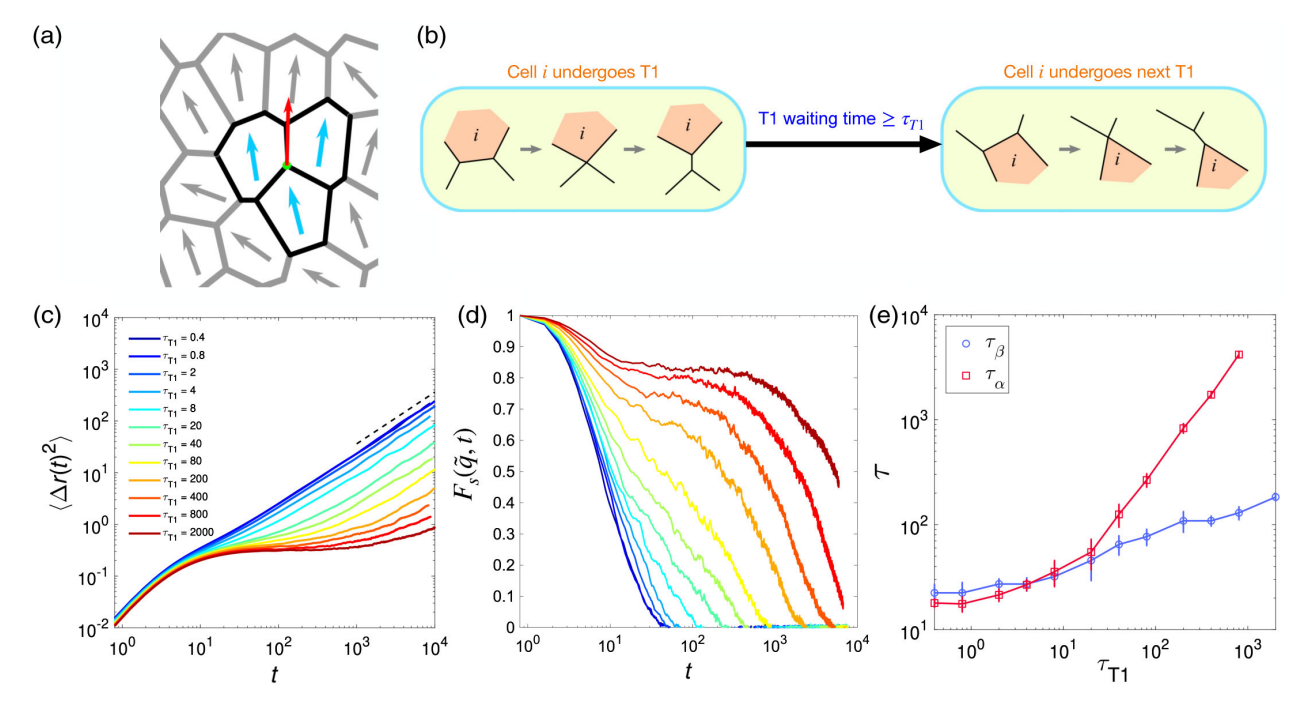


FIG. 1. Increased persistence of T1 events in the dynamic vertex model (DVM) slows down cell dynamics. (a) In the DVM, the dynamics of a vertex depends on motility of adjacent cells (also see the Appendix A). (b) Introducing the "T1 stalling timescale" τ_{T1} which represents the time duration over which T1 transitions are stalled for any cell i. Consequently, τ_{T1} becomes the lower bound for the waiting time observed between successive T1 events involving cell i. This happens due to the stochastic dynamics of cellular junctions. (c) Mean-square displacements (MSDs) of the cell centers for fixed $v_0 = 1.6$ at different τ_{T1} . The dashed line, with a slope of 1 on a log-log scale, indicates the diffusive behavior. (d) Self-intermediate scattering function $F_s(\tilde{q}, t)$ for the same v_0 at different τ_{T1} . Here, $\tilde{q} = \pi/\sqrt{A_0}$, where $\sqrt{A_0}$ is the unit of length in our model. (e) β - and α -relaxation timescales, τ_{β} and τ_{α} , respectively, as functions of τ_{T1} .

Each cell in the DVM behaves like a self-propelled particle with motility force v_0 [53,59,60] acting on the geometric cell center. The total active force on vertex i is

$$\mathbf{f}_{i}^{\text{active}} = v_0 \tilde{\mathbf{n}}_{i},\tag{4}$$

where $\tilde{\mathbf{n}}_i$ is the direction of average active force on vertex *i* [Fig. 1(a) and Appendix A].

B. Implementation of T1 stalling time

The most crucial ingredient in our model is a "T1 stalling timescale." We introduce this as a tunable time period τ_{T1} for which we limit T1 processes for any cell in our simulated tissue. A technical advantage of vertex-based models for cells over particle- or Voronoi-based models is the ability to explicitly control the connectivity between edges, vertices, and cells in the tissue. A T1 transition consists of a local topological change in the network as illustrated in Fig. 1(b). Whereas previous implementations treat these events as instantaneous or a fixed embargo timer [48,49,52,54,56,61,62], here we implement a method of executing T1s in a history-dependent manner. For each cell, a timer δt_c is kept which records the time elapsed since the last T1 transition involving the cell. This timer measures the single-cell waiting time between successive T1 events.

Initially, cells are seeded with random values of this timer δt_c , chosen from a uniform distribution $[0,\tau_{\rm T1}]$. Subsequently, in the simulation, an edge adjacent to the cell undergoes a T1 if and only if two conditions are met: (i) The length of the edge is shorter than a threshold $l_{\rm min}=0.1$ times the simulation length unit, and (ii) $\delta t_c > \tau_{\rm T1}$. This rule introduces an effective persistence governing intercalations of cells and is illustrated schematically in Fig. 1(b). Such persistence originates from the inherent delays associated with the stochastic cell intercalation observed in living tissues [13,16,27–29]. The tissue remains a confluent monolayer (where cells do not overlap and no gaps exists between them) throughout the entire simulation run within this implementation of the vertex model.

III. RESULTS

A. Dynamical slow down in cellular motion due to persistence in T1 events

The primary focus of this study is the interplay of motility and the inherent T1 stalling timescale and how it affects collective tissue behavior. Hence, our starting point is a tissue that is solidlike when cell motility is absent $(v_0 = 0)$. In the vertex model, this corresponds to the cell shape index $p_0 < p_0^*$, where $p_0^* = 3.81$ [56] is the

transition point between solidlike and fluidlike behaviors in the limit of $v_0 = 0$. Therefore, the majority of results presented hereon are at a fixed $p_0 = 3.6$. In Fig. 9 of Appendix B, we show that results at other values of p_0 do not alter our overall finding. A recent concurrent study [63] reaches the same conclusions using a similar vertex model implementation for delayed T1s and varying p_0 .

In order to understand the effects of τ_{T1} on cell dynamics, we start in the fluid phase of the model [corresponding to a high motility ($v_0 \gg 0.6$) at this p_0]. To quantify the cell dynamics, we compute the mean-square displacements (MSDs), $\langle \Delta r(t)^2 \rangle$ of cells [Figs. 1(c), 8(a), 9(a), and 9(b) in Appendix B], and the self-intermediate scattering function $F_s(\tilde{q},t)$ [Figs. 1(d), 9(d), and 9(e) in Appendix B], a standard measure in glassy physics to quantify structural relaxation (see Appendix B for details of the calculation). When τ_{T1} is small, cell motion is ballistic $[\langle \Delta r(t)^2 \rangle \propto t^2]$ at short times and at long times behaves diffusively ($\propto t$). This corresponds to the fluidlike behavior when T1 events are nearly instantaneous which is extensively studied [37,48,49,51]. As expected in this motility-driven fluid, here, $F_s(\tilde{q},t)$ decays sharply with a single relaxation timescale [Fig. 1(d)]. However, at a larger choice of τ_{T1} , the MSD develops a "plateau" after the early ballistic regime and requires an increasingly longer time to become diffusive as τ_{T1} is increased. The appearance of this plateau is indicative of the onset of kinetic arrest, i.e., glasslike behavior. This shows up as a two-step relaxation in terms of $F_s(\tilde{q},t)$ [Fig. 1(d)]. These features of MSD and $F_s(\tilde{q},t)$ persist regardless of the choice of p_0 (Fig. 9 in Appendix B). In glassy physics [64–67], the origin of the two-step relaxation is attributed to β relaxation, taking place at intermediate times when each cell jiggles inside the cage formed by its neighbors, which is also responsible for the plateau in MSD, and α relaxation, taking place at later times when a cell is uncaged and undergoes large-scale motion to make the MSD rise after the plateau.

We quantify the glassy behavior by extracting the timescale of β relaxation, τ_{β} [68], by locating the point of inflection in the MSD curve on a log-log plot [see Appendix B and Fig. 8(c)]. The timescale τ_{α} associated with α relaxation can be extracted from $F_s(\tilde{q},t)$ (see Appendix B). In Fig. 1(e), we plot the dependence of τ_{β} and τ_{α} on τ_{T1} [see also Fig. 9(f) in Appendix B for results of τ_{α} at different p_0]. For low τ_{T1} (fast T1s), the two timescales coincide, indicating τ_{T1} has no discernible effect on the dynamics, but for $\tau_{T1} > 20$ the difference between the two timescales grows dramatically. This provides a characteristic timescale where the hindrance of T1s causes effective caged motion and kinetic arrest in cells. This behavior is reminiscent of the onset of glassy behavior in supercooled liquids; the natural question is whether introducing a T1 stalling timescale merely provides another route leading to a conventional glassy state, similar to, e.g., decreasing the temperature. To answer this question, we quantify the dynamical heterogeneity in states undergoing kinetic arrest due to the time constraint and compare with more conventional glassy states obtained by lowering of v_0 at short τ_{T1} .

We compute the four-point susceptibility $\chi_4(t)$, a standard measure of dynamical heterogeneity in glassy systems [68,69]. For nearly instantaneous T1s [Fig. 2(a)], the tissue behaves similar to a conventional supercooled glass as v_0 is decreased: $\chi_4(t)$ exhibits a peak which shifts toward larger times with decreasing v_0 . Together with the increase in the peak magnitude of $\chi_4(t)$, these results indicate that the length scale and timescale associated with dynamic heterogeneity become increasingly larger due to lowering of v_0 , which plays the role of an effective temperature [53]. Using the peak value χ_4^* [Fig. 2(c)], the glass transition can be located at $v_0 \approx 0.8$. In contrast, the behavior of $\chi_4(t)$ for a large τ_{T1} is drastically different. Here, $\chi_4(t)$ develops a plateau [70,71] over decades in time [Fig. 2(b)]. Here, the width of the plateau is significantly broader than in the low $\tau_{\rm T1}$ regime. Further, hindering T1s here also reduces the dependence of dynamic heterogeneity on v_0 , and the peak value of χ_4^* [Fig. 2(c)] no longer exhibits pronounced peaks as a function of v_0 . This indicates that the T1 stalling timescale dominates over motility and acts as the ratelimiting factor in determining cell rearrangements. This analysis reveals that, while the high τ_{T1} regime becomes kinetically arrested, it does so in a manner distinct from reducing temperature in conventional supercooled liquids. Here, the characteristic dynamical timescale is largely controlled by τ_{T1} rather than the effective temperature in the system. Therefore, the glassy behavior in the tissue is directly controlled by τ_{T1} , and the resultant glassy states possess a lower degree of dynamic heterogeneity compared to the conventional glassy states.

B. Intermittency in T1 events points to a dynamic regime distinct from a conventional glass

Given that the origin of a growing dynamic heterogeneity in glasses is attributed to the highly intermittent motion of individuals [67], we explicitly investigate how intermittency of T1 rearrangements depends on v_0 and τ_{T1} . For this, we measure the single-cell waiting time (τ_w) , which is defined as the length of time periods between successive T1 events involving a single cell [illustrated in Fig. 1(b)]. By tracking all neighbor exchanges, we maintain a time-dependent list of single-cell waiting times, denoted by $\{\tau_w^i(t)\}$, i=1,2,...,N, which contains the instantaneous values of the waiting times for all the cells. From this list, we define an instantaneous average waiting time $\bar{\tau}_w^{inst}(t) = (1/N)\tau_w^i(t)$ [Figs. 2(d) and 2(e)] per cell at time t. We also consider distributions of all the observed waiting times for all the cells, denoted by $P(\tau_w)$ (Fig. 10 in Appendix B).

When τ_{T1} is small, T1 rearrangements are nearly unconstrained [Fig. 2(d)]. When the motility is high, $\bar{\tau}_w^{\text{inst}}(t)$ exhibits steady fluctuations about a mean value that is slightly larger than the lower bound set by τ_{T1} . As motility

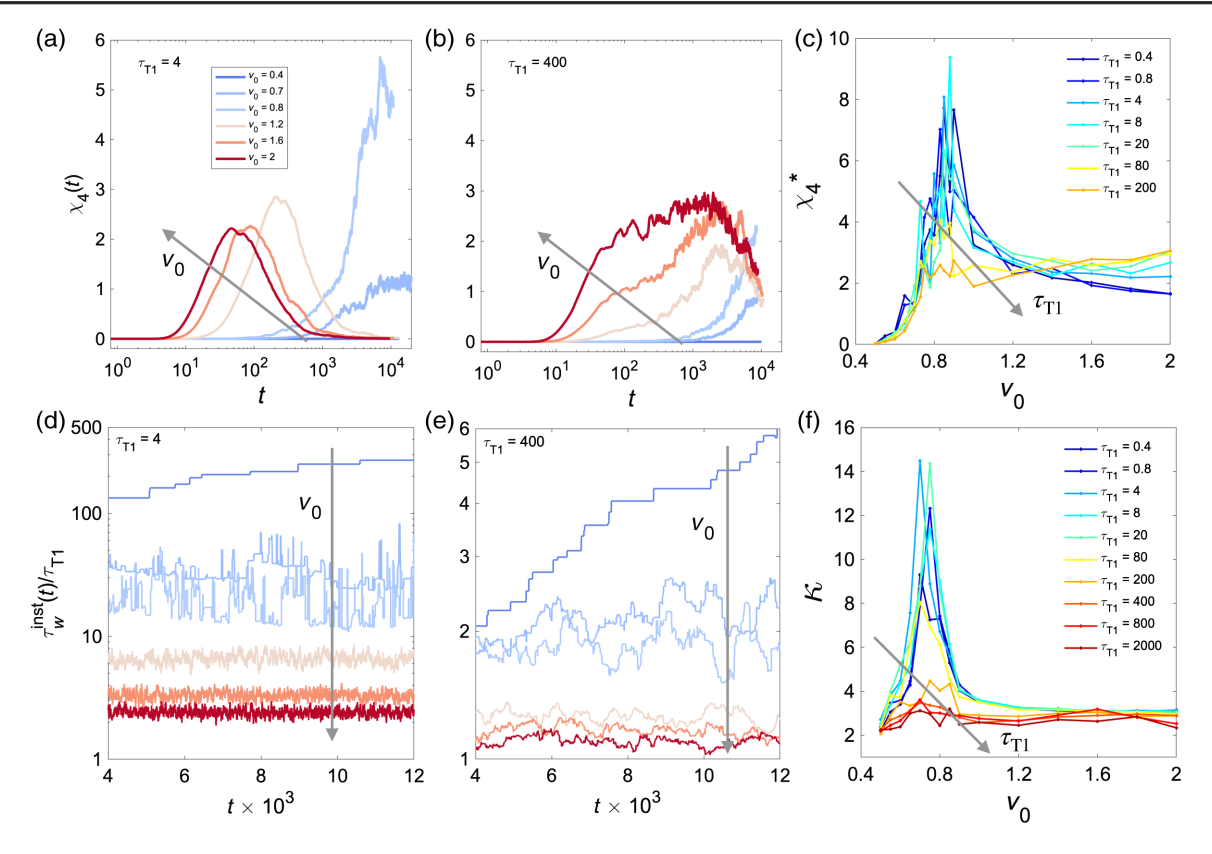


FIG. 2. Persistence in T1 events introduces variable degrees of dynamic heterogeneity and drives intermittency of rearrangements. (a), (b) Four-point susceptibility $\chi_4(t)$ for different v_0 at two different τ_{T1} . (c) Peak value of χ_4 denoted as χ_4^* vs v_0 . (d),(e) Time series of the instantaneous average of the waiting times of all cells, given by $\bar{\tau}_w^{inst}(t)$, for the parameters corresponding to (a) and (b). (f) The kurtosis κ of the observed values of $\bar{\tau}_w^{inst}$, as a function of v_0 .

is lowered, neighbor exchanges become less frequent, hence increasing $\bar{\tau}_w^{\rm inst}(t)$ overall. At even lower motility, near the glass transition, the dynamics becomes highly intermittent, and, consequently, T1 events are separated by a broad distribution of waiting times (Fig. 10 in Appendix B), and multiple rearrangements can take place simultaneously akin to avalanches [69]. Deeper in the glass phase, $\bar{\tau}_w^{\rm inst}(t)$ increases slowly over time, reminiscent of the aging behavior observed in glassy materials [67,69].

At large τ_{T1} [Fig. 2(e)], the intermittent fluctuations, observed around the glass transition regime in Fig. 2(d), are dampened significantly. Here, $\bar{\tau}_w^{\text{inst}}(t)$ always fluctuates around a mean value until motility becomes too low. The low-motility behavior of $\bar{\tau}_w^{\text{inst}}(t)$ remains unaffected by an increase in τ_{T1} .

To further characterize the nature of fluctuations in the instantaneous waiting times and the intermittency, we follow the variation of kurtosis κ extracted from the distributions of the waiting times given by $P(\tau_w)$ (Fig. 10 in Appendix B). In the short $\tau_{\rm T1}$ regime, $P(\tau_w)$ decays with heavy power-law tails for $v_0 \sim 0.6{-}0.8$ [Fig. 10(a) in Appendix B], and here κ vs v_0 exhibits a very pronounced peak [Fig. 2(f)]. This is also where the glass transition takes place upon decreasing the single-cell motility. At higher motilities, away from the glass transition point, $\kappa \approx 3$ corresponding to Gaussian fluctuations which is

apparent from the nature of $P(\tau_w)$ [Fig. 10(a) in Appendix B]. However, at sufficiently large τ_{T1} , $P(\tau_w)$ [Fig. 10(b) in Appendix B] becomes relatively narrow for all motilities and κ remains close to 3. This is a clear indication that large τ_{T1} reduces the intermittency of cell rearrangements near the glass transition. These evidences consolidate our observations and conclusions from the behavior of dynamic heterogeneity. Next, we analyze the interplay between the T1 stalling time and the observed mean waiting times.

C. Universal scaling separates fast and slow glassy regimes

The mean waiting times $\langle \tau_w \rangle$ obtained from $P(\tau_w)$ exhibit strong dependence on both v_0 and τ_{T1} [Fig. 3(a)]. We compare $\langle \tau_w \rangle / \tau_{T1}$, which always remains larger than unity and varies by orders of magnitude. This variation is more than 1000-fold at small τ_{T1} . However, as τ_{T1} increases, $\langle \tau_w \rangle / \tau_{T1}$ approaches unity and depends weakly on v_0 . This behavior suggests a universal scaling

$$\frac{\langle \tau_w \rangle}{\tau_{\text{T1}}} = f(\tau_{\text{T1}} v_0^z). \tag{5}$$

In Eq. (5), f(x) is the dynamical crossover scaling function with $x = \tau_{\text{T1}} v_0^z$.

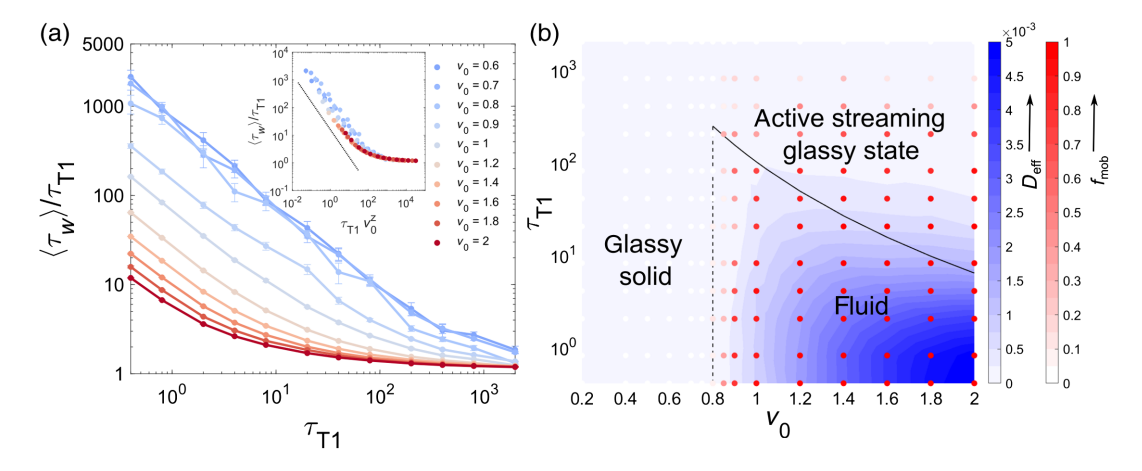


FIG. 3. Universal scaling of waiting times and phase diagram of cell dynamics. (a) Mean waiting times, scaled by τ_{T1} , $\langle \tau_w \rangle / \tau_{\text{T1}}$ as a function of τ_{T1} at different v_0 . Inset: scaling collapse of $\langle \tau_w \rangle / \tau_{\text{T1}}$ with the scaling variable $x = \tau_{\text{T1}} v_0^z$ and exponent $z = 4.0 \pm 0.1$. The black dotted line is a guideline for the power law of x^{-1} . (b) The phase diagram on the $v_0 - \tau_{\text{T1}}$ plane shows three different regimes of cell dynamics along with approximate phase boundaries. The black dotted line represents an approximate boundary between the glassy solid and the fluid phase. The black solid line is the phase boundary predicted by the crossover scaling function given by Eq. (5). The heat map represents the values of effective diffusivity D_{eff} , and the intensities of the color of overlaid circular symbols represent the values of f_{mob} , the fraction of mobile cells with net displacements of at least two cell diameters.

Replotting the data using Eq. (5), we find good scaling collapse with exponent $z=4.0\pm0.1$ [Fig. 3(a), inset]. This scaling relation uncovers two distinct regimes. For small x, $f(x)\sim x^{-1}$, which implies $\langle \tau_w\rangle \propto v_0^{-z}$. We refer to this as the *fast* rearrangement regime. For large x, $f(x)\to 1$, indicating a *slow* rearrangement regime where $\langle \tau_w\rangle \propto \tau_{T1}$ and independent of v_0 . The transition between the two regimes occurs at $x=x^*\approx 100$, corresponding to a scaling relation of $\tau_{T1}=x^*v_0^{-z}$ that constitutes the boundary separating these two rearrangement regimes.

The dynamics in the fast regime is not hindered by $\tau_{\rm T1}$ and is primarily driven by the effective temperature $T_{\rm eff} \propto v_0^2/D_r$ [53]. For high values of v_0 in this regime, the motile forces are sufficient to overcome the energy barrier associated with T1 transitions; however, as v_0 drops below $v_0^* \approx 0.8$, the tissue enters into a *glassy solid* state where cell motions become caged.

In the slow regime, τ_{T1} dominates the dynamics, as it is the longest timescale in the system and, therefore, the ultimate bottleneck to rearrangements. This leads the mean waiting times for T1 events to depend linearly on τ_{T1} while being insensitive to motility. In addition to glassy behavior, which is a source of nonequilibrium fluctuations, here, τ_{T1} constitutes another possible route that can take the system out of equilibrium, effectively slowing down the dynamics.

Here, the uncaging timescales (τ_{α}) grow with τ_{T1} [Fig. 1(e)] but remain quite finite, as in a highly viscous or *glassy fluid*. This kind of dependence of tissue relaxation on the rate of T1 events is also reported recently by Krajnc and co-workers [55] using a 3D vertex model. They show, using a Monte Carlo implementation of T1 transitions, that if active T1 events are allowed in a tissue at a rate k_{T1} , independent of the energy barriers, the tissue viscosity

 $\eta \propto k_{\rm Tl}^{-1}$. Since away from a glass transition τ_{α} and η both are similar measures of relaxation [72] and $\tau_{\rm Tl} \equiv 1/k_{\rm Tl}$, our observed linear growth of τ_{α} with $\tau_{\rm Tl}$ [Fig. 1(e)] resembles the above behavior of tissue viscosity.

D. Phase diagram of cellular dynamics

Based on these observations, the phase diagram on the $v_0 - \tau_{T1}$ plane [Fig. 3(b)] can be categorized into three phases: (i) a glassy solid phase, (ii) a fluid phase, and (iii) an unusual *active streaming glassy state (ASGS)*, which is discussed in depth below. The approximate solid-fluid phase boundary is given by peak positions in κ [Fig. 2(f)] and χ_4^* [Fig. 2(c)] and effective diffusivity $D_{\rm eff}$ [Appendix B and Figs. 3(b) and 8(b)] [53]. The boundary between fluid and the ASGS phase is given by the crossover scaling [Eq. (5)] between the slow and fast regimes.

The ultralow D_{eff} values in the ASGS phase resemble a solid more than a fluid. However, the finite τ_{α} [Fig. 1(e)] and the nature of MSDs (Figs. 8 and 9 in Appendix B) and waiting times (Fig. 10 in Appendix B) indicate that these states are solidlike only for timescales less than τ_{T1} . Furthermore, the eventual transition to diffusive motion (at times $\gg \tau_{\rm T1}$) is due to a small population of fast-moving cells. To understand this peculiar form of fluidity, we quantify the fraction of relatively fast-moving or mobile cells, given by f_{mob} (for details see Appendix B). As expected, f_{mob} is large and close to 1 for *fluid* and zero for glassy solid. This also holds true for other values of p_0 [Fig. 9(c) in Appendix B]. However, in the ASGS, f_{mob} decreases slowly as τ_{T1} increases yet always remains finite. These results indicate that the ASGS always includes states with a heterogeneous mixture of fast and slow cells. This is

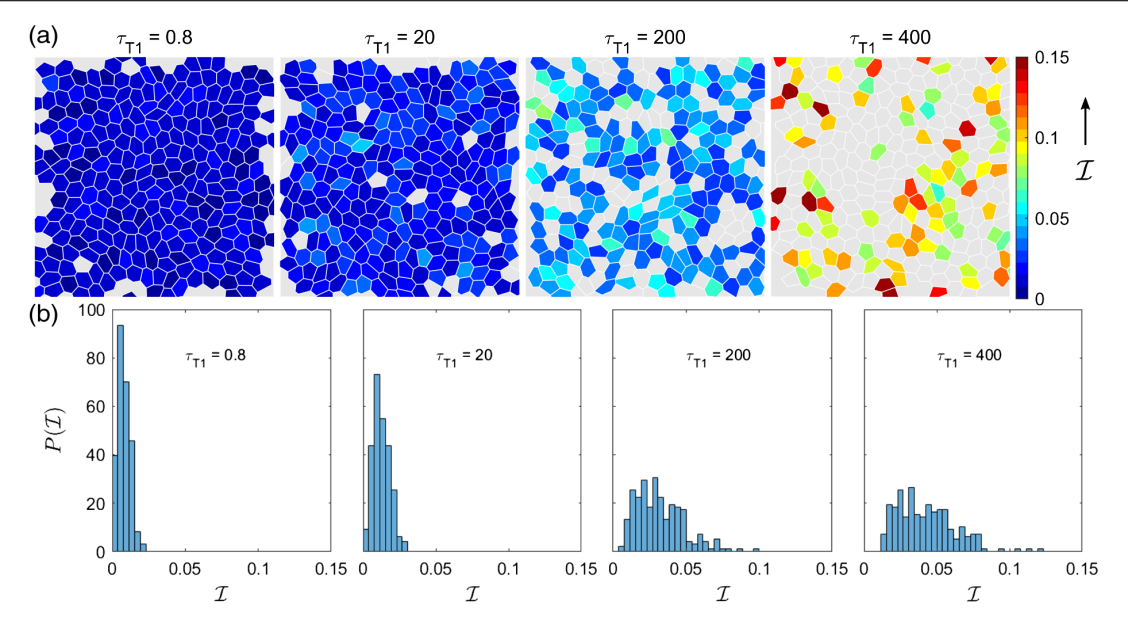


FIG. 4. Fast cells organize into streams as T1 stalling time increases. (a) Simulation snapshots for four different τ_{T1} values at fixed $v_0 = 1.6$. Only the fast cells are shown (net displacement $d_{\infty} \gtrsim 2$ cell diameters; see Appendix B for details) are color coded according to their intercalation efficiencies, defined as $\mathcal{I} = d_{\infty}/n_{\text{T1}}$, where n_{T1} is the net T1 count. (b) Distributions of cell-level \mathcal{I} values, for different τ_{T1} .

a signature of an emergent spatial-temporal heterogeneity which we try to understand next.

E. Self-organization of fast-moving cells leads to the emergence of cellular streams

We observe that depending on the phase they belong to (solid, fluid, or ASGS), the fast cells exhibit different degrees of neighbor exchanges. This can be quantified by defining a single-cell intercalation efficiency

$$\mathcal{I} = d_{\infty}/n_{\mathrm{T1}},\tag{6}$$

where d_{∞} is the net displacement and n_{T1} is the net T1 count for a given cell in the entire simulation (see Appendix B for more details). This quantity captures the difference between reversible T1 events that do not help cells to move away from its neighborhood and irreversible T1 events that effectively allow cells to uncage and move. We find that for the fast cells \mathcal{I} increases with increasing $\tau_{\rm T1}$ at a fixed motility [Fig. 4(a)]. This is consistent, because short τ_{T1} offers a higher tendency of reversing T1 transitions, compared to when τ_{T1} is large. Simultaneously, the spatial distribution of the fast cells becomes increasingly heterogeneous and streamlike at large τ_{T1} . The distributions of \mathcal{I} [Fig. 4(b)] also reflect this change, as they become broader and heavy tailed, with a two- to fivefold increase in the mean efficiency $\bar{\mathcal{I}}$ as τ_{T1} goes up. These results indicate that, as T1 events are limited at large τ_{T1} , only a few mobile cells are able to undergo T1 and they become increasingly irreversible and induce effective migration. The fast cells also exhibit mutual spatiotemporal alignment that grows rapidly with τ_{T1} as reflected in the distribution of their mutual alignment angles [Fig. 11(a) and see Appendix B for details]. We also extract an overall alignment probability ϕ_a [defined in Appendix B, data shown in Fig. 11(b)] which is insensitive to τ_{T1} at small motilities but remains large due to collective vibrations in a solidlike tissue [53]. ϕ_a becomes increasingly dependent on τ_{T1} at higher motilities, which shows that stalling T1s for a prolonged time period alone can induce alignments, but such alignments can result migratory potential and streamlike behaviors only when cell motility becomes sufficiently large. This observation also justifies the location of the ASGS on the phase diagram shown in Fig. 3(b).

These self-organized cell streams are visualized in cell trajectories [Fig. 5(a), top]. When τ_{T1} is low, they are uniformly distributed and randomly oriented. However, as τ_{T1} increases, they become sparse and grouped into streamlike collectives. These collectives are increasingly correlated and persistent at larger τ_{T1} . Here we use a time interval much smaller than the corresponding β -relaxation timescales to compute the displacement vectors of cell centers. Therefore, this type of collective behavior occurs even before a majority of the cells uncage. To quantify the spatial correlations arising during streaming, we adapt a quantity \vec{V} [73], computed in the comoving frame of a given cell, which represents the average velocities at different locations around it. Collective migratory behavior shows up as vectors of similar length and direction near the cell, whereas solid or fluidlike behavior results in isotropic organization of vectors of uniform sizes. In Fig. 5(a), bottom, signatures of collective motions are absent when τ_{T1} is small but gradually appear with an

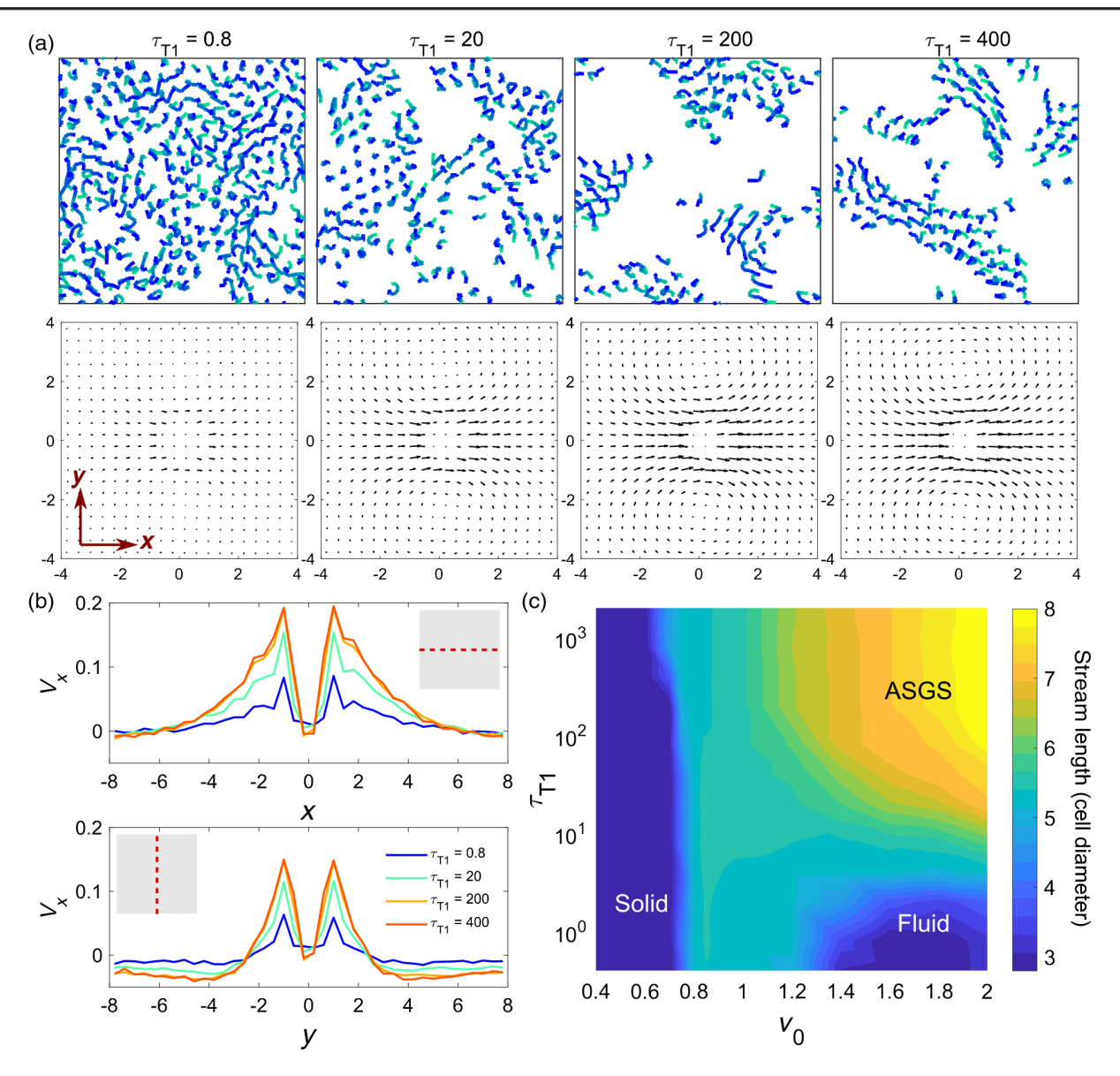


FIG. 5. Visualization and characterization of cell streaming. (a) The individual cell trajectories at different τ_{T1} and fixed $v_0=1.6$. Top row: cell trajectories for a short time period. Colors change from green to blue to mark cell positions progressively forward in time. Trajectories are shown only for the cells that travel 80% of average cell diameter or more distance in this time window. Bottom row: average velocity field \vec{V} around any cell corresponding to each panel in the top row. Here, the reference cell is always at the origin, its velocity vector pointing from left to right. (b) Correlation of cell motions is shown by plots of V_x , the x component of \vec{V} , along two lines parallel to the x axis (top) and the y axis (bottom), respectively. These two lines are also illustrated as dotted lines in the insets. (c) The typical length of cell streams, estimated from the plot of V_x along the x axis [top in (b)], shown as a color map as a function of v_0 and τ_{T1} . Here, we define the length or width of the stream, as we move away either along the x or y direction from the origin, respectively, to be the distance between the points where V_x falls off below a fixed value $V_x^* = 0.05$, suitably chosen to calculate the stream sizes. The color map of stream lengths varies significantly across the three phases as encountered in Fig. 3, while the stream widths vary very little between three and four average cell diameters.

increase in τ_{T1} as the sizes and orientations of the vectors become more correlated along the direction of motion and remain uncorrelated along the direction perpendicular to it. Such anisotropic vector fields are hallmarks of cellular streaming [73,74] that involves high front-back correlations [Fig. 5(b), top] and low left and right correlations [Fig. 5(b), bottom]. The decay of these correlations also provides

the size of streams. The stream lengths extracted from the front-back correlations [Fig. 5(b), top] are shown as a color map as function of v_0 and τ_{T1} in Fig. 5(c). The stream length remains small (approximately 3 times the average cell diameter) in the solid and fluid phases, while it varies up to 8 times average cell diameter and nicely highlights the distinctive dynamics of ASGS. The stream width, on the

other hand, remains constant throughout (approximately 3–4 times the average cell diameter). A closer analysis of the spatial-temporal velocity correlations reveal that these streams are reminiscent of a *leader-follower* behavior [40,44,75–77]. Here, the strength of correlations increases with τ_{T1} [Fig. 11(c) in Appendix B].

F. Increased persistence of T1 events results in effective cell-cell cohesion

Having demonstrated the organization of collective multicellular streams, a remaining question is the physical mechanism underlying streaming. Since streaming behavior must rely on cells becoming stuck to one another over some time, we next focus on the dynamical evolution of cell-cell contacts. The delays between successive T1 events introduced by τ_{T1} in our model tune the stability of cell-cell contacts. Two neighboring cells maintain an effective adhesion for a time period equal to τ_{T1} or longer, depending on the time evolution of the shared junction. In simulations, we have direct access to the lifetimes of the cellular cohesion events or an effective dynamic adhesion timescale τ_{ad} from the cell-cell adjacency information. Alternatively, we can measure these timescales using cell tracking.

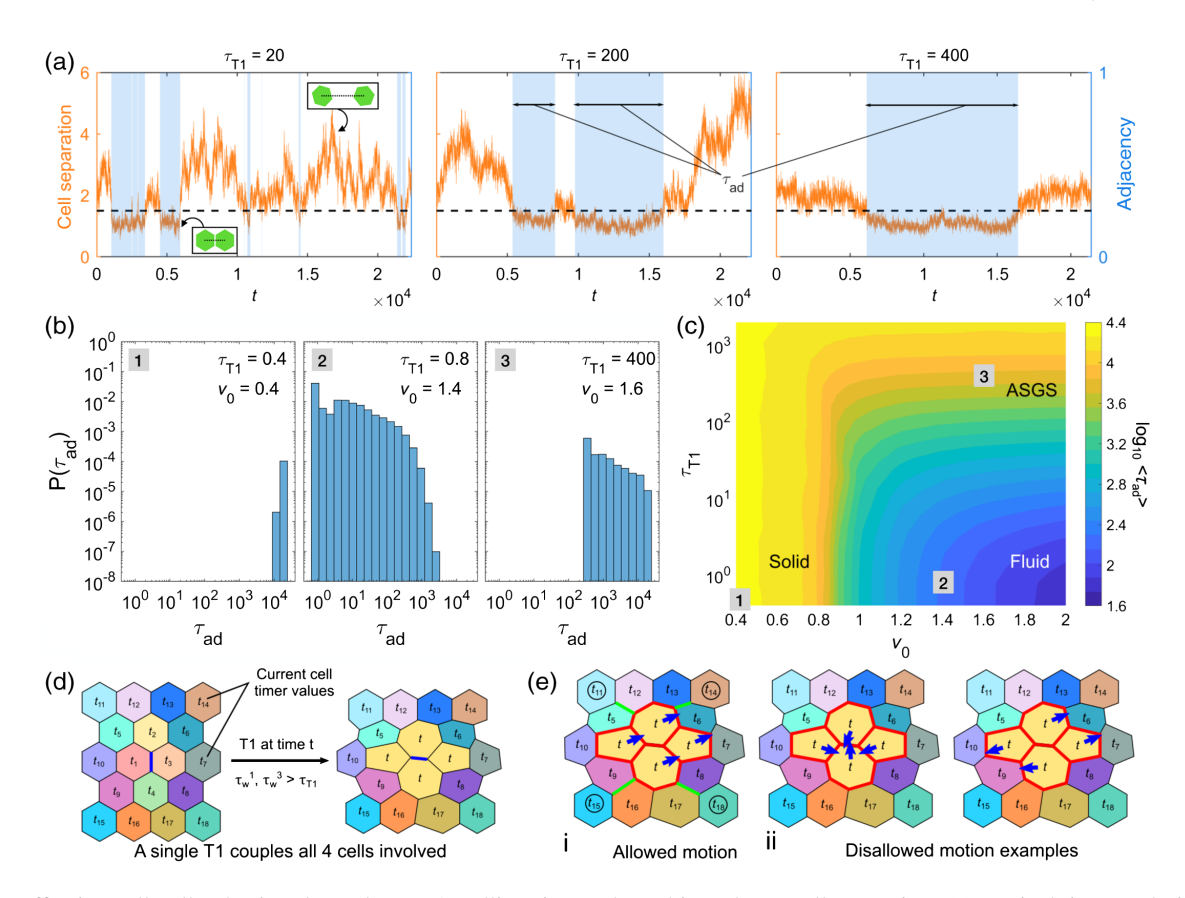


FIG. 6. Effective cell-cell cohesion depends on T1 stalling timescale and introduces cell streaming. (a) Typical time evolution of the adjacency (blue) and center-to-center distance (orange) of a pair of cells. Adjacency is 1 when the pair are immediate neighbors (i.e., sharing a junction) and zero when they are not neighbors. Width of the blue shaded areas indicates periods for which they form a cohesive pair, defined as the effective adhesion timescale τ_{ad} . The time evolution of cell-cell separation provides another measure of τ_{ad} , given by the periods for which the separation remains below a suitably chosen fixed threshold of 1.5 times an average cell diameter. Examples are shown for different τ_{T1} at fixed $v_0 = 1.6$ which show that cell pairs can undergo multiple events of cohesion, and the two different methods of determining τ_{ad} agree quite well. See Fig. 11(d) in Appendix B for more data on comparison of these two methods. (b) Probability distribution functions of the effective adhesion timescales $P(\tau_{\rm ad})$, shown at different combinations of v_0 and $\tau_{\rm T1}$. (c) A color map of $\langle \tau_{ad} \rangle$, estimated from cell adjacency information as a function of τ_{T1} and v_0 . (d),(e) Proposed mechanism of how effective cohesion can lead to cell streaming. (d) shows a tissue patch of 18 cells, each with a different timer $\delta t_i = t_i$ recording the time elapsed since the last T1. Cells 1 and 3 (sharing the blue colored junction) undergo T1 at time t as their respective waiting times exceed τ_{T1} . This T1 not only resets the timers on cells 1 and 3, it also resets the timers on nearby cells 2 and 4, because they now become neighbors after the T1. This resetting introduces an effective adhesion in several cell pairs and forbids another T1 event involving the junctions colored in red for a period at least τ_{T1} . (e) shows the consequence of this effect. These four cells can now only move coherently [case (i)] with types of motions forbidden, as illustrated here [case (ii)]. Thus, this cluster of four cells acts as a nucleator for a cell stream, that can grow in length as any of the neighboring cells, marked by circles [case (i)], can join the cluster via T1 transitions involving the junctions colored green [case (i)] and propagate the streaming.

Figure 6(a) illustrates the time evolution of cell-cell cohesion for multiple cell pairs which become neighbors at some point using these two techniques. Figure 6(b) shows the probability distributions of the effective adhesion times, $P(\tau_{ad})$, in different regions of the phase diagram. When τ_{T1} is small, cell-cell contacts are frequent but short lived. Then $P(\tau_{ad})$ is very narrow for low motilities, with a single peak at $\tau_{\rm ad} \approx \tau_{\rm total}$, the total simulation time, as expected in the glassy solid state. Increase in motility widens $P(\tau_{ad})$ in the fluid state, while the peak at τ_{total} disappears. At high motility, if τ_{T1} becomes large, the system enters the ASGS. Here, $P(\tau_{ad})$ remains wide and is maximum at $\tau_{\rm ad} \approx \tau_{\rm T1}$. An important feature is that the variance of τ_{ad} is always large for high-motility states, indicating a heterogeneity in the remodeling of cell-cell contacts. The mean adhesion times $\langle \tau_{ad} \rangle$, shown as a color map in Fig. 6(c), also reflect these trends. In addition, $\langle \tau_{ad} \rangle$ strongly depend on τ_{T1} in the ASGS, which indicates the existence of a state where stability of cohesive cell clusters can be tuned over a broad range [see also Fig. 11(d) in Appendix B]. This is reminiscent of the previous suggestions [39–45,77,78] that streaming cells observed in cancer tumors are typically associated with a range of strengths of cell-cell adhesion, from weak to intermediate. This is exactly what we observe here as well.

This analysis reveals that different glassy regimes [Fig. 3(b)] can be distinguished based on measuring the characteristic time of cell-cell cohesion and its statistical distribution $P(\tau_{\rm ad})$. For example, consider two different glassy states, one with a large $\tau_{\rm T1}$ and one with small motility. In terms of conventional measures, both states exhibit glassy features (vanishing $D_{\rm eff}$ and large χ_4); however, our work predicts that the state with a large $\tau_{\rm T1}$ should have a broadly distributed $P(\tau_{\rm ad})$ compared to a conventional glassy state.

The emergence of cell streaming from the effective cellcell cohesion is an amplified tissue-level response to the persistence memory introduced by the stalling of the T1 events. This can be shown by inspecting the consequences of a single T1 event in our model [Fig. 6(d)]. It not only resets the timers on the two cells swapping the shared junction, but also resets timers on nearby cells that now become neighbors after the swap. These events introduce a cohesive four-cell unit that is stable for a time period of at least τ_{T1} . This time restriction also sets a natural lower bound to the τ_{ad} 's, as reflected in Fig. 6(b). A consequence of this effective cohesion is that these four cells can now move coherently only for a period τ_{T1} or more [Fig. 6(e)]. The only way this cluster can move is via T1 transitions involving junctions at the periphery, as illustrated in Fig. 6(e)-case (i). This also allows this cluster to grow into a stream only when τ_{T1} is optimal, because very frequent or rare T1 events would not be useful. That is why we see a drop in f_{mob} [Fig. 3(b)] and saturation of τ_{ad} [Fig. 6(c)] as τ_{T1} becomes very high. The movements of such streams are always unidirectional at any given time instance which gives rise to an effective leader-follower behavior [Fig. 11(c) in Appendix B]. One possible way to test whether synchronized T1 rearrangements can lead to streaming in the physiological context is to use high-resolution cell tracking, e.g., as described in Ref. [22]. Stabilization of four-cell units for a finite time period following T1 events is, however, a common observance in biological tissues and has been quantified [13,16].

G. Predictions for *Drosophila* pupa development

Cell intercalations in our model are randomly oriented and spatially uncorrelated. Such unpolarized cell intercalations have recently been observed in the *Drosophila* notum during the early pupal stage [16]. Experimental evidence indicates that random fluctuations in junction lengths are necessary for unpolarized cell intercalations. It is also observed that the rate of intercalation drops as the pupa ages, coinciding with an increase in junctional tensions. In Ref. [16], T1 rates and junctional tensions are studied by perturbing the myosin-II activity via the Rho-signaling pathway. Overexpression of Rho-kinase (Rok-CAT) leads to an increase in myosin-II activity and junctional tensions, which stiffens the junctions to lower the rate of rearrangements. On the other hand, a downregulation of Rok by RNA interference (Rok-RNAi) lowers junctional myosin-II activity and tensions, which, in turn, enhances the T1 rates. Similarly, tuning the activity within the DVM corresponds to changing the single-cell motility v_0 , which also controls the active fluctuations at cellcell junctions. At the same time, tuning τ_{T1} allows for direct control on T1 rates in certain regions of the phase space as pointed out before (Sec. III C). Now the question is whether we can understand the mechanism of how the T1 rates and junctional tensions get coupled under the influence of these two parameters.

We observe that the experimentally measured T1 rates of the three cases—the wild type, Rok-CAT, and Rok-RNAi—can be quantitatively mapped onto the predicted T1 rates from the DVM as a function of v_0 and τ_{T1} [Fig. 7(a)]. Thus, values for v_0 and τ_{T1} for these three scenarios can be represented by different contours with their respective experimentally observed T1 rates on the $v_0 - \tau_{T1}$ plane [Fig. 7(a)]. We predict a $v_0 - \tau_{T1}$ value pair for the wild-type pupa on this plane, from which two diverging paths corresponding to the two perturbations can be forged that conform to the experimentally observed trends of junctional tensions [Fig. 7(b)]. The agreement of the predicted fold change of junctional tensions from the wild type to Rok-CAT is quantitative, while that to the Rok-RNAi is qualitative. Interestingly, both of these predicted paths involve changes in both v_0 and τ_{T1} which are beyond the fluctuating tension-based model used by Curran and coworkers to interpret their results. In their model, junctional tensions are considered to undergo Gaussian fluctuations with a characteristic autocorrelation time. In DVM, we do not make any such assumption, and the junctional tension is

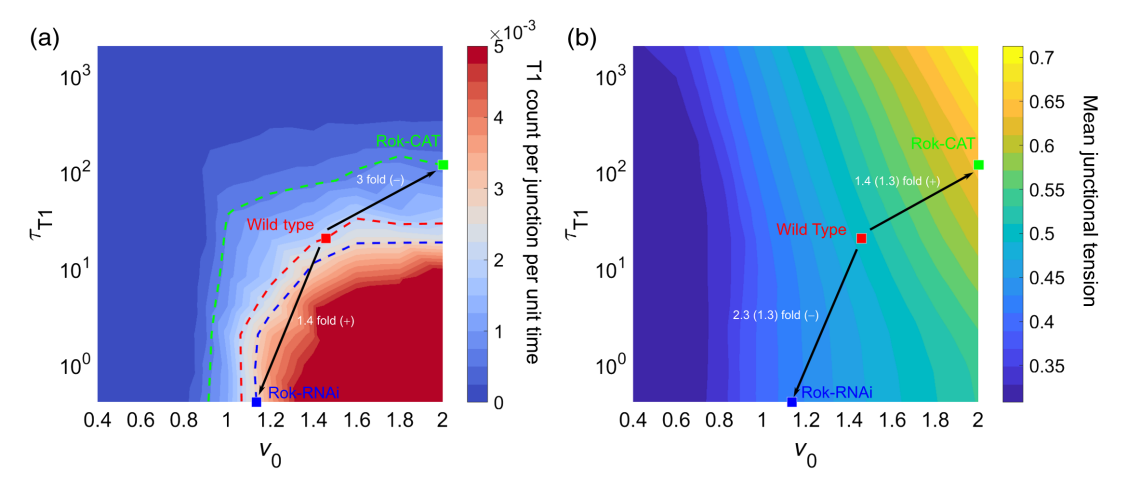


FIG. 7. DVM makes a qualitatively consistent prediction of the trends of T1 rates and junctional tension observed during the development of Drosophila pupal notum by Curran and co-workers in Ref. [16]. (a) Color map of T1 rates predicted by DVM. Contours representing the experimental T1 rates are marked by dashed lines (wild-type, red; Rok-CAT, green; Rok-RNAi, blue). To map the experimental T1 rates from Ref. [16] on our model-predicted T1 rates, we make the former dimensionless (see Appendix A for details). (b) Color map of tensions predicted by DVM. Both panels show the DVM-predicted transition paths from the wild-type to the perturbation scenarios on the $v_0 - \tau_{T1}$ plane. We also show the experimentally observed fold changes of T1 rate (a) and tension (b) in the two perturbations from the wild type. In (b), the numbers in parentheses are the corresponding fold changes predicted by DVM for tensions. + or - within parentheses indicates increase or decrease, respectively.

an emergent quantity that arises from the balance of the restoring forces on any shared junction due to cell shape mechanics and force from the active motility of the cells. Thus, DVM overcomes this limitation of the vertex model in Ref. [16] and adds a more realistic interpretation for the mechanism of the junctional tension-T1 rate coupling in a tissue. DVM predicts that the perturbations done to the Rho pathway could be associated with changes in both the active forces associated with cell motility and the cell-level persistence of T1 events. Therefore, both the single-cell parameters v_0 and $\tau_{\rm T1}$ would be necessary to understand the mechanics of this tissue development. Both of these parameters are included here as intrinsic to a single cell, which also brings in the premise of a cell-level control of local dynamical processes in tissues.

Furthermore, in our previous work with human lung tissues, we have encountered situations where both the junctional tensions and T1 rates vary proportionately with v_0 , when τ_{T1} remains low, and this can be captured within the conventional version of the DVM [38]. In the *Drosophila* pupal notum, however, we see a departure from this conventional behavior of cell arrangements. This is where the roles of the persistence of T1 events and τ_{T1} become crucial. From wild type to Rok-CAT, DVM predicts an increase in v_0 accompanying an increase in tension while the T1 rate decreases. From wild type to Rok-RNAi, on the other hand, DVM predicts a drop in v_0 while tension diminishes, but the T1 rate increases. In both of these paths, activity incorporated as v_0 seems to remain the mechanism controlling tension. However, the T1 rate seems to decouple with v_0 that cannot be described by the conventional vertex-based models where T1 rates are fundamentally correlated with activity. The current version of DVM becomes relevant which describes these trends in T1 rate through tuning of τ_{T1} .

Finally, DVM predicts the wild-type tissue and the tissue resulting from Rok-RNAi to be in the fluid regime, which is consistent with the observed uncorrelated T1 events that do not alter the overall shape of the tissue. On the other hand, the Rok-CAT system exhibits a large drop in T1 rates from the wild type and DVM consistently predicts it in the ASGS, where T1 events are strongly limited. The Rok-CAT system also involves a reduced number of reversible T1 events, which means the rearrangements that happen lead to permanent changes in cell neighborhoods. This is also a common feature of the ASGS. Thus, our analysis brings out the power of this simple framework, which can help us understand the nature of tissue fluidity in different tissue states.

IV. DISCUSSION AND CONCLUSION

To model the collective dynamics of confluent epithelial cells, we introduce an inherent timescale (τ_{T1}) for cells to undergo rearrangements based on the important observation that T1 events in real tissues do not occur instantaneously. When τ_{T1} is short compared to other timescales in the model, we recover a glass transition, occurring way below the motilities large enough to overcome the energetic barriers that cause a cell to become caged. Near this glass transition, we observe highly intermittent cell motion, as well as neighbor exchanges concomitant with growing dynamical heterogeneity.

However, when τ_{T1} grows, we discover a rich dynamical regime where the system appears glassy on timescales

governed by $\tau_{\rm T1}$ but becomes fluidized at longer times. Compared to the glass transition mentioned above, this regime has a completely different kind of heterogenous glassy behavior characterized by the disappearance of the conventional glass-fluid boundary and the appearance of spatially distributed pockets of fast and slow cells. The origin of this new glassy behavior stems from the effective cell-cell cohesion caused by the inability to undergo local cellular rearrangements. Surprisingly, this local frustration actually serves to enhance collective migration by facilitating streamlike patterns, reminiscent of leader-follower behavior, albeit without any explicit alignment interactions between cells. Interestingly, this connection diminishes as mean effective adhesion times saturate when persistence of rearrangements becomes too low or too high [Fig. 11(d) in Appendix B]. Therefore, the cell-cell contacts need to be dynamic but optimally stable to maintain the streaming mode. These results are consistent with the existing biological mechanisms of cell streaming [40,77] and shed new light on the nature of cell-cell adhesion associated with cell streaming in cancerous tissues [40].

The glass transition for small τ_{T1} is consistent with previous observations with cell-based models [53,59]. Similar behaviors are also observed in other models of biological tissues by tuning the rates of cell growth [79] or division and death [80–82]. The emergence of collective streamlike behavior as a result of tuning τ_{T1} is also reminiscent of the recent observations that increasing the persistence of motility timescales can lead to swirl-like correlations in active-matter models [83–86].

Experimental dynamical measurements in cell layers often have limited time durations. When measuring dynamic heterogeneity $\chi_4(t)$ with limited time windows, it is, therefore, possible that a cell layer in an active streaming glassy state cannot be easily distinguished from a conventional fluid state near a glass transition (e.g., when $\tau_{\rm T1}$ is low). Here, we suggest some alternative measurements that can distinguish ASGS from a conventional glassy fluid state. In experiments where individual T1 events between pairs of cells can be tracked over time, then the intercalation efficiency \mathcal{I} (defined in Sec. III E) can be used. The corresponding theoretical predictions can be found in Sec. III E and Fig. 4. In cases where experimental limitations prevent the tracking of individual T1s, but the cell displacement field can be obtained (e.g., by using particle image velocimetry), we propose that multicellular streams in ASGS can be captured by the analysis of the spatial correlation function of the cell displacement field (detailed in Sec. III E and Fig. 5). Furthermore, we suggest a simple measurement for the overall polarization of a cellular stream [Figs. 5 and 11(a) in Appendix B] can reveal its front-back polarity. The alignment probability ϕ_a [Fig. 11(b) in Appendix B] can then be used as an order parameter for ASGS. In situations where neither T1 tracking nor long-time displacements of cells are available but live cell nuclei staining can be performed, we suggest the measurement of the effective cell-cell adhesion time $\tau_{\rm ad}$ (detailed in Sec. III F). In this case, the variance in $P(\tau_{\rm ad})$ can be used as a signature to distinguish between ASGS and a conventional fluidlike tissue (Fig. 6).

Also, in prior implementations of the vertex model [45,60], when an additional alignment is included between the single-cell polarization and its migration velocity, cells can form collective flocks where their polarization vectors are persistently aligned. Interestingly, such flocks can also contain cellular packs that are spatially anisotropic—qualitatively similar to cell streams in the ASGS. However, in ASGS, the cell polarizations do not develop explicit orientational order in the polarity field $\{\hat{n}_i\}$. While structurally similar, it will be interesting to study whether ASGS and cellular flocks share the same degree of spatial fluctuations. Moreover, it would be interesting to introduce the T1 timescale to the flocking model and understand the interplay between the persistent time of a "liquid-flock" state [60] and τ_{T1} .

On the other hand, the ASGS partially shares some similarities with previous observations in glassy or supercooled liquids as well. For example, a similar kind of global slowing of the dynamics has been recovered previously by one of us in a square-well fluid with tuned interparticle bond lifetimes [87]. Accompanying the slowing down in the ASGS, the structural relaxation becomes slaved to the imposed persistence on cell rearrangements as τ_a increase following a power law with τ_{T1} . This dependence is very much in line with the observed power-law dependence of τ_{α} or viscosity η on shear rate near glass transition in sheared glassy materials [88–92]. The flat wide $\chi_4(t)$ observed in the ASGS appears to arise also in attractive colloids where the mechanism could, in essence, be similar—from clusters of particles that are stuck together and are mobile at low densities [70,71]. On the other hand, the streamlike motions in the ASGS happens in the absence of any dynamic heterogeneity, and this sets it apart from stringlike cooperative motion observed in a 3D supercooled liquid [93], which is a direct consequence of dynamic heterogeneity. Note that a totally different kind of large-scale collective streaming has been observed within the vertex model by controlling the persistence of single-cell motion with open or ring-shaped boundaries [94].

The effective adhesion picture that emerges from our study is also supported by the recent observations regarding polarized intercalations in extending the germ band of a *Drosophila* embryo [22]. Oscillation in the levels of adhesion protein E-cadherin at the remodeling junction has been deemed necessary for successful intercalations, while inhibition of this oscillation by preventing E-cadherin endocytosis leads to its sustained enrichment at junctions and a decrease in successful T1 events. Our predictions reverse engineer this effect by limiting the rate of T1 events, which leads to an increase in effective cell-cell adhesion

and stability of junctions. Therefore, increasing the E-cadherin levels at the junctions and reducing its fluctuation would be a biochemical way of achieving this junction stability and, consequently, a control mechanism for the T1 stalling timescale. Regulation of the rates of E-cadherin endocytosis or an overexpression of E-cadherin near the junctions about to remodel could be two such mechanisms [22]. Furthermore, myosin-II flows directed to the junctions have been suggested as upstream controllers of E-cadherin enrichment at T1 associated junctions during Drosophila germ-band extension [20,21] and pupal notum development [16]. Reference [22] further correlates myosin-II activity with the temporal oscillation of E-cadherin at the remodeling junctions. Thus, controlling the signaling pathways that govern these myosin-II flows, such as the Rho-Rok pathway, could be other possible ways cells regulate neighbor exchanges and the T1 stalling timescale.

The unusual nature of the *active streaming glassy state* has a multitude of implications. The slow but finite structural relaxation gives the material a tunable viscosity which can be highly useful for preparation of biology-inspired sheetlike objects of controllable stiffness [95,96]. The control of T1 rate can be potentially translated to gene-level control of the signaling [97] associated with developmental events and disease conditions that strongly depend on cell intercalations, e.g., body-axis extension and kidney-cyst formation [2], respectively. This might even allow design of organisms with programmable development [98] or one with controlled disease-spreading rates.

Finally, the effective adhesion introduced as a result of delayed rearrangement addresses a long-standing shortfall of the static vertex model. In the vertex model interaction energy [Eq. (2)], an increase of the target shape index p_0 corresponds to an increase in the cell-cell adhesion [48,61], while at the same time it has been shown that higher p_0 also corresponds to fluidlike tissue behavior [56]. The reason for the emergence of this solid-fluid transformation was clarified recently [57,58]. At higher p_0 values, the edge tensions on cell-cell junctions vanish, making it unable support rigidity. However, this alone suggests stronger cell-cell adhesion enhances fluidity—an assertion that may seem counterintuitive. The reason for this apparent disconnect is that previous vertex models capture only the static energetic contribution of cell-cell adhesion but do not include the dynamical aspect of cell-cell adhesion, i.e., increased adhesion causes rearrangements to slow down. Here, as we demonstrate, the inclusion of a T1-time delay provides a natural way to introduce the additional viscous timescale that governs the dynamics of junction remodeling.

ACKNOWLEDGMENTS

We thank Chandan Dasgupta for insightful comments and discussions. This work was supported by the Indo–U.S. Virtual Networked Joint Center project titled "Emergence and re-modeling of force chains in soft and biological

matter" No. IUSSTF/JC-026/2016 (A. D., S. S., and D. B.), by the Northeastern University TIER 1 Grant (A. D. and D. B.), by the Centre for Theoretical Biological Physics at Northeastern University (A. D.), and by the National Science Foundation (NSF) DMR-2046683 (D. B.). We also acknowledge the support of the Northeastern University Discovery Cluster. S. S. acknowledges support through the JC Bose Fellowship (JBR/2020/000015) from the Science and Engineering Research Board, Department of Science and Technology, India.

APPENDIX A: MODEL DETAILS

1. Active cell motility in DVM

The explicit form of the active force on any vertex i depends on the motility force contributions from the adjacent cells:

$$\tilde{\mathbf{n}}_i = \sum_{c \leftrightarrow i} a_c \mathbf{n}_c,\tag{A1}$$

where $a_c = l_c/(2z_i \sum_{c \leftrightarrow i} l_c)$ is the weight associated with cell c adjacent to the vertex i, l_c is the total length of the edges shared by vertex i and cell c, z_i is the connectivity at vertex i, and the factor 2 takes care of double contributions from the same cell. This averaging scheme is different than the recent approaches using a flat average of active forces on adjacent cells [37,81,99] and ensures that the active force on vertex i is dominated by the cell sharing the longest edges attached to i. The polarization of the self-propulsion on cell c is given by $\mathbf{n}_c = (\cos \theta_c, \sin \theta_c)$, where the polarization angle θ_c is perturbed only by a white noise [100–104]:

$$\frac{d\theta_c}{dt} = \zeta_\theta,\tag{A2}$$

where the ζ_{θ} is a Gaussian white noise with zero mean and variance $2D_r$ which sets the repolarization timescale for the cells in our model given by $1/D_r$. We use a fixed D_r for all cells throughout the present study.

2. Simulation details

Our simulations are overdamped dynamics of N=256 cells periodic boundaries along both x and y directions. We use $\sqrt{A_0}$ as the unit of length, K_PA_0 as the unit of energy, and ζ/K_P as the unit to measure time t in our simulations. The vertex positions are updated by solving Eq. (1) using Euler's scheme. Our dynamical simulations are initialized from random Voronoi configurations which are subjected to energy minimization using the conjugate-gradient algorithm. All simulations are done in the Surface Evolver program [105] with a fixed equilibrium cell area $A_0 = \bar{A} = 1$ (\bar{A} , the mean cell area) and time step of integration $\Delta t = 0.04$. We run each of our simulations for approximately 10^6 steps and collect data for subsequent analyses after the tissue

properties, like the mechanical energy reaches steady state. Simulations take typically 10^5 steps to reach steady state. We scan the following parameter space: $v_0 \in [0.2, 2]$ and $\tau_{T1} \in [0.4, 2000]$ at a fixed $D_r = 0.5$. For each combination of v_0 and τ_{T1} we perform 10–20 independent simulations.

APPENDIX B: ANALYSIS OF CELL TRAJECTORIES

1. Measuring junctional tension

Tensions arise in the vertex model due to mismatch between the actual cell perimeters and the equilibrium perimeter. It can be defined in terms of the preferred scaled perimeter or target cell shape index p_0 . We calculate tension on any junction shared between cells i and j by

$$T_{ij} = (p_i - p_0) + (p_j - p_0),$$
 (B1)

where p_i and p_j are respective scaled cell perimeters, measured during the simulation.

2. Determination of τ_{β}

We extract the β -relaxation timescale from any given MSD vs t plot by locating the minimum in the time derivative of MSD given by $d \ln[\langle \Delta r^2(t) \rangle]/d \ln(t)$ [106].

Plots of this time derivative for MSDs shown in Fig. 1(b) are shown in Fig. 8(c).

3. Analysis of self-intermediate scattering function $F_s(\tilde{q}, t)$

We use the following definition of self-intermediate scattering function: $F_s(q,t) = \langle e^{i\mathbf{q}\cdot\Delta\mathbf{r}(t)} \rangle$, where q is the wave vector corresponding to our length scale of choice and the angular brackets represent ensemble average and averages over angles made by \mathbf{q} and $\Delta \mathbf{r}(t)$, cell displacement vectors for time delay t. The latter average reflects the azimuthal symmetry of the scattering function with respect to the orientation of wave vector **q**. Conventionally, emphasis is given to how $F_s(q=2\pi/\sigma,t)$ decays as a function of time, where σ is the interparticle particle separation for configurations with particles just touching. However, we choose to focus on analyzing the behavior of $F_s(\tilde{q},t)$ at a more restrictive wave vector $\tilde{q}=\pi/\sigma$, corresponding to a length scale of two cell diameters. The reason for this is a technical one: Since the degrees of freedom in the DVM are the vertices rather than the cell centers, the cell centers (calculated at every step based on vertices) can exhibit unusual fluctuations even when cells are completely caged. The current choice of \tilde{q} allows us to consider relaxations where these artificial fluctuations

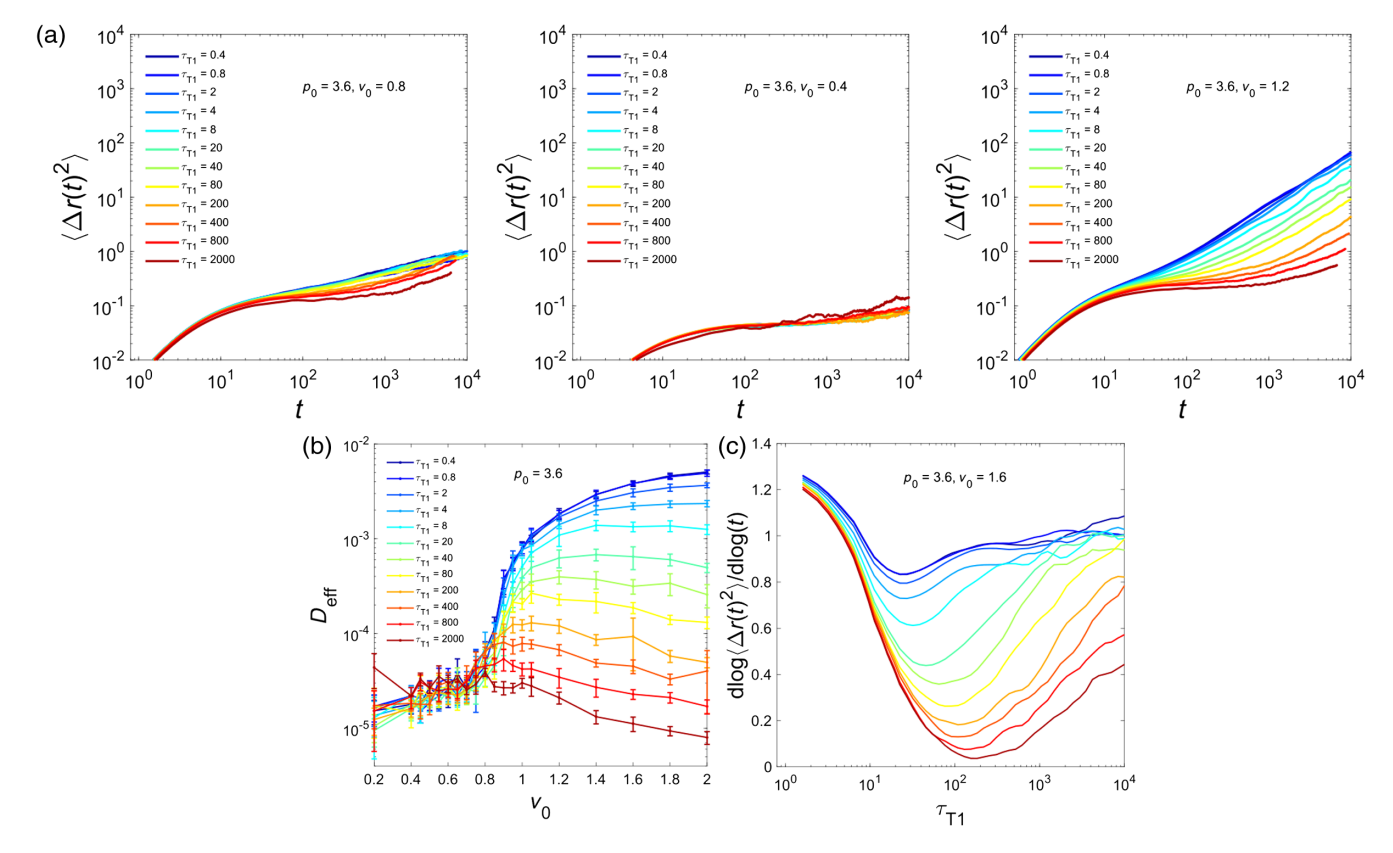


FIG. 8. (a) MSDs for three different v_0 at different τ_{T1} . (b) Effective diffusivity $D_{\rm eff}$ as a function of v_0 at different τ_{T1} . Error bars are SEM for n=10 independent simulations. (c) Time derivative of MSD for $v_0=1.6$. Data shown for $p_0=3.6$.

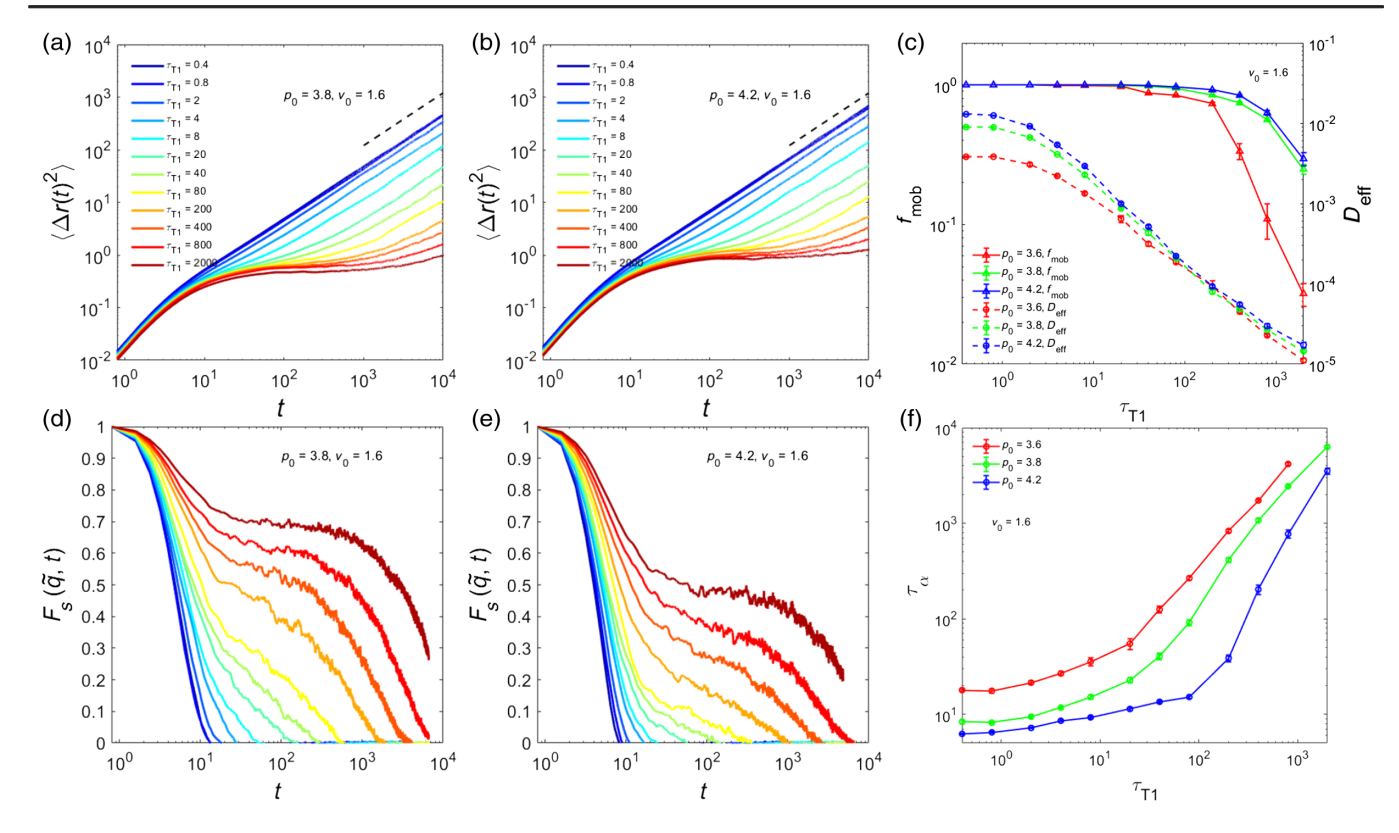


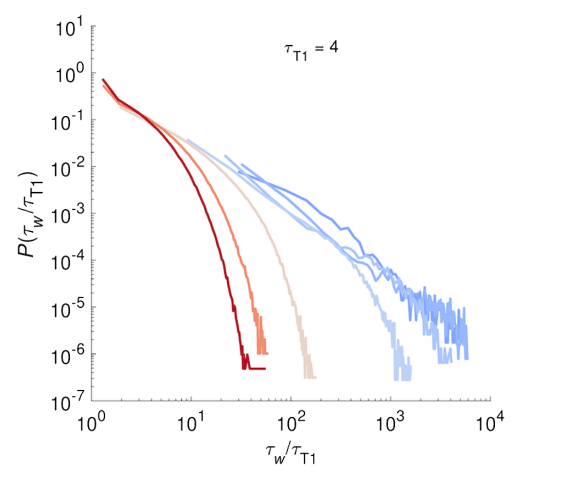
FIG. 9. (a),(b) MSDs and (d),(e) $F_s(\tilde{q},t)$ for $v_0=1.6$ with (a),(d) $p_0=3.8$ and (b),(e) $p_0=4.2$. (c),(f) Comparison of relaxation and transport properties across three different p_0 's for fixed $v_0=1.6$. (c) $D_{\rm eff}$ and $f_{\rm mob}$ as a function of $\tau_{\rm T1}$. (f) τ_{α} vs $\tau_{\rm T1}$ as a function of $\tau_{\rm T1}$. Error bars are SEM for n=10 independent simulations.

contribute much less. To eliminate contributions from any local or global drift, we consider temporal changes in nearest-neighbor separations as $\Delta \mathbf{r}(t)$ instead of pure displacements of cell centers.

We define the α -relaxation timescale τ_{α} as follows: $F_s(\tilde{q}, t = \tau_{\alpha}) = 0.2$, following the definition used recently by another cell-based model study on similar tissues [107].

4. Calculation of four-point dynamic susceptibility $\chi_4(t)$

We calculate $\chi_4(t)$ as the variance of the two-point correlation function Q(t) [68] which is widely used in the glassy physics to characterize caging and uncaging dynamics: $\chi_4(t) = N[\langle Q(t)^2 \rangle - \langle Q(t) \rangle^2]$. The two-point correlation function is defined as $Q(t) = (1/N) \sum_{i=1}^N w[|\mathbf{r}_i(t) - \mathbf{r}_i(0)|]$,



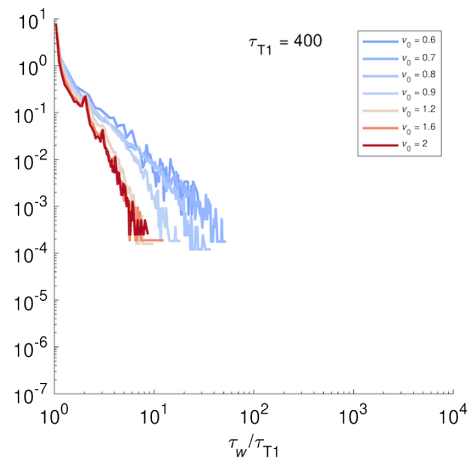


FIG. 10. Here, we show normalized probability distribution functions of measured waiting times τ_w between successive T1 events involving individual cells at different v_0 and two different τ_{T1} values. The distributions at small τ_{T1} and v_0 near glass transition are much broader with heavy power-law tails, while they are always quite narrow and without heavy tails for large τ_{T1} value. The colors follow the legends shown in the right.

where w(x) is a window function that is unity for $x \le r_c$ and zero otherwise. Therefore, Q(t) represents the fraction of cells that moves by a distance r_c or more after time t, from its initial position at t=0. We fix $r_c=\sqrt{A_0}$, the typical size of one cell as the characteristic distance. The angular brackets here represent the ensemble average over thousands of steady-state time windows chosen from 10–20 independent simulations. Each of these time windows are of length 2.5– 8×10^5 steps. Because each time step in our simulation is 0.04

simulation time units, this allows us to plot $\chi_4(t)$ in Fig. 2 up to at least $t = 10^4$ simulation time. We use a similar protocol to calculate all the ensemble averages associated with the dynamical quantities, like MSD and $F_s(\tilde{q}, t)$.

5. Definition of quantities associated with mobility

We use several order parameters to describe different regimes of cell dynamics in our model tissue. Below, we

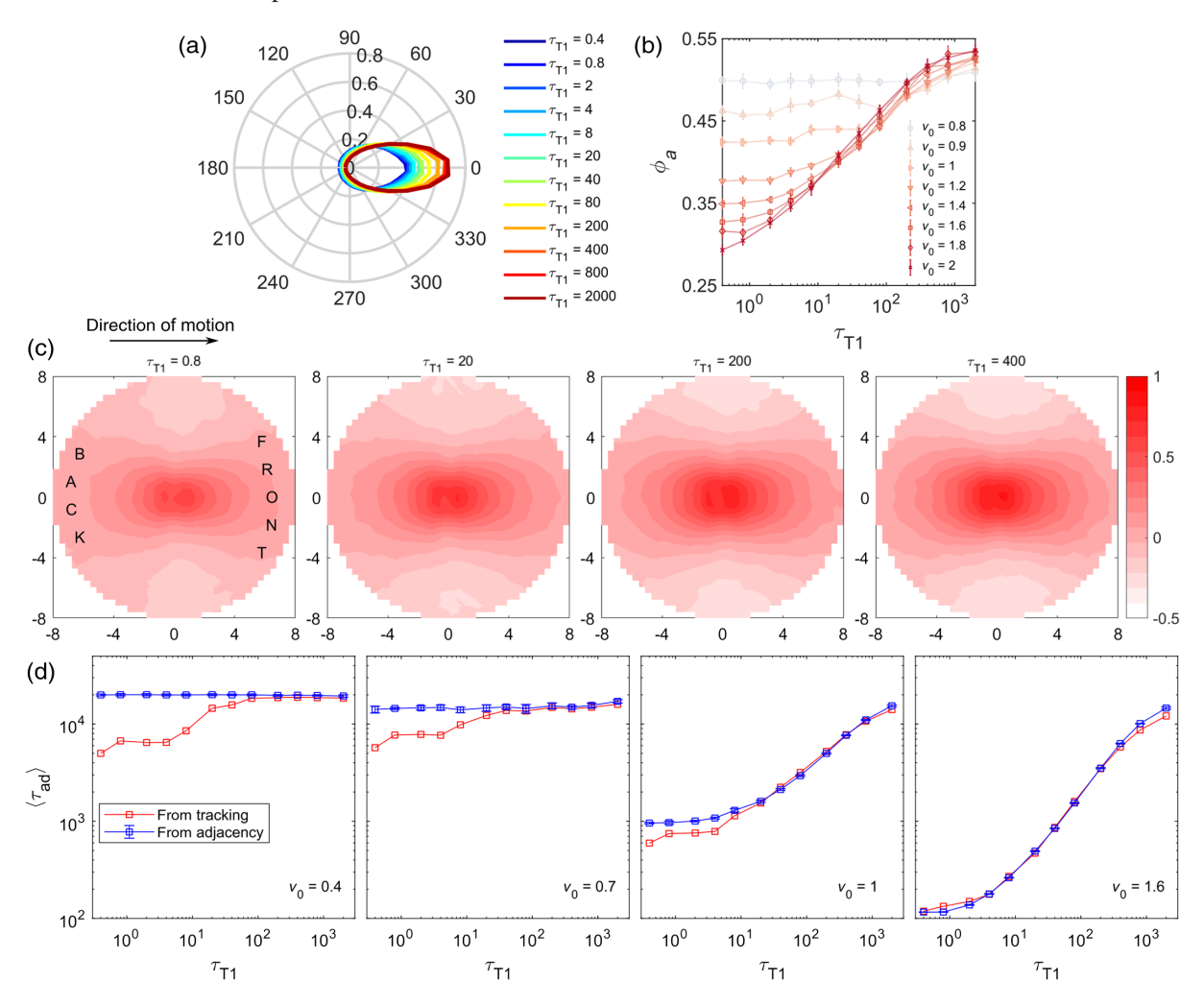


FIG. 11. Characterization of cell-cell alignment and front-back correlation in the direction of motion. (a) Distributions of angles (shown as polar plots) between displacement vectors of a pair of cells separated by less than two cell diameters. This is calculated for cells with $\mathcal{I} \geq \bar{\mathcal{I}}$, the mean intercalation efficiency per cell in the tissue. Data shown for $v_0 = 1.6$. (b) Average cell alignment probability ϕ_a as a function of τ_{T1} for different v_0 . The error bars are standard deviations of the mean for 10–20 samples. (c) Spatial directional correlation of cell motions around the fast cells in the tissue. We follow a recent analysis [76] that probes how the motion of any two cells are correlated as a function of both their distance and the direction from one cell, chosen as reference, to another. We find that this directional correlation, shown above for different τ_{T1} values at $v_0 = 1.6$, is low and nearly uniform in all directions and decays very sharply within 1–2 cell diameters for short τ_{T1} . As τ_{T1} increases, we see the correlation contours getting longer-ranged, polarized, and elongated along the direction of motion of the reference cell. These features are classical signatures of leader-follower behavior. For $\tau_{T1} \geq 100$, we see very strong, anisotropic directional correlations that remain significant even at six cell diameters away from the reference cell. This approximate correlation length is consistent with that found from vector field analysis of cell streaming. These results show that the fast cells play major roles driving the cellular streaming observed for very large τ_{T1} . (d) Comparing mean effective adhesion timescale $\langle \tau_{ad} \rangle$, estimated from cell adjacency information (blue squares) and tracking of cell centers (red squares), as a function of τ_{T1} at different v_0 . This highlights the robustness of the estimation from cell tracking which can be employed to analyze experimentally tracked cell trajectories.

define them one by one. We define effective diffusivity by $D_{\rm eff}=D_s/D_0$, where $D_s=\lim_{t\to\infty}\langle\Delta r(t)^2\rangle/4t$, the long-time self-diffusion coefficient, and $D_0=v_0^2/2D_r$, the free diffusion coefficient of a single isolated cell. D_s is computed using the value of mean-square displacement at the largest t allowed in our simulation.

To define the fraction of mobile cells $f_{\rm mob}$, we follow individual cell MSD and define the net displacement of a cell: $d_{\infty} = \lim_{t \to \infty} \sqrt{\langle \Delta r^2(t) \rangle}$. Then, we find out the number of cells $N_{\rm mob}$ that have $d_{\infty} \gtrsim 2$ cell diameters. Finally, $f_{\rm mob} = N_{\rm mob}/N$. This definition is consistent with the definition of mobile particles used in Ref. [108].

6. Analysis of orientation alignment in cell trajectories

To capture the orientational order and spatial organization of fast cells, we concentrate on the cells with intercalation efficiency $\mathcal{I} \geq \bar{\mathcal{I}}$, the mean intercalation efficiency. This gives us a list of fast cells. Then, we consider the whole simulation trajectory and calculate the probabilities of the angle θ_a between the instantaneous displacement vectors of any cell pair chosen from our list of fast cells, where the cell-cell separation is less than or equal to two cell diameters. We consider all possible cell pairs satisfying this criterion and pool all the θ_a to generate the probability density function $P(\theta_a)$. We define the net alignment probability ϕ_a by the following:

$$\phi_a = \int_{-t_c}^{t_c} P(\theta_a) d\theta_a, \tag{B2}$$

where $t_c = 30^{\circ}$.

7. Connecting model results to previous experimental observations

In the DVM, the T1 rate is measured as the number of T1 events per junction per simulation time unit. It is expressed as a dimensionless count. In order to compare the trends of T1 rates as a function of the various model parameters of DVM, it is convenient to express the experimentally measured T1 rates in Curran et al. [16] also as a dimensionless quantity. We choose the typical myosin turnover timescale [16] as the unit of time with which to nondimensionalize T1 rates reported in Ref. [16]. Then, the rescaled experimental T1 rates are mapped on the DVM heat map [Fig. 7(a)] by comparing the fold changes in the experimental data vs the fold changes in DVM. We also compare the trends of predicted vs measured tensions as a function of the model parameters of DVM. However, the tensions in Ref. [16] are not measured in units of force but in terms of the recoil velocity of the ablated junctions. Therefore, we make a comparison of the fold changes in our predicted tension values corresponding to the mapped T1 rates with the experimentally measured fold change in recoil velocities.

- [1] K. D. Irvine and E. Wieschaus, Cell Intercalation during Drosophila Germband Extension and Its Regulation by Pair-Rule Segmentation Genes, Development 120, 827 (1994).
- [2] E. Walck-Shannon and J. Hardin, *Cell Intercalation from Top to Bottom*, Nat. Rev. Mol. Cell Biol. **15**, 34 (2014), review article.
- [3] L. Carvalho, P. Patricio, S. Ponte, C.-P. Heisenberg, L. Almeida, A. S. Nunes, N. A. M. Araújo, and A. Jacinto, Occluding Junctions as Novel Regulators of Tissue Mechanics during Wound Repair, J. Cell Biol. 217, 4267 (2018).
- [4] R. J. Tetley, M. F. Staddon, D. Heller, A. Hoppe, S. Banerjee, and Y. Mao, *Tissue Fluidity Promotes Epithelial Wound Healing*, Nat. Phys. 15, 1195 (2019).
- [5] M. Tada and C.-P. Heisenberg, Convergent Extension: Using Collective Cell Migration and Cell Intercalation to Shape Embryos, Development 139, 3897 (2012).
- [6] M. Rauzi, Cell Intercalation in a Simple Epithelium, Phil. Trans. R. Soc. B 375, 20190552 (2020).
- [7] D. L. Weaire and S. Hutzler, *The Physics of Foams* (Oxford University Press, New York, 2001).
- [8] S. S. Lienkamp, K. Liu, C. M. Karner, T. J. Carroll, O. Ronneberger, J. B. Wallingford, and G. Walz, Vertebrate Kidney Tubules Elongate Using a Planar Cell Polarity—Dependent, Rosette-Based Mechanism of Convergent Extension, Nat. Genet. 44, 1382 (2012).
- [9] A. Shindo and J. B. Wallingford, *Pcp and Septins Compartmentalize Cortical Actomyosin to Direct Collective Cell Movement*, Science **343**, 649 (2014).
- [10] R. Etournay, M. Popović, M. Merkel, A. Nandi, C. Blasse, B. Aigouy, H. Brandl, G. Myers, G. Salbreux, F. Jülicher, and S. Eaton, *Interplay of Cell Dynamics and Epithelial Tension during Morphogenesis of the Drosophila Pupal Wing*, eLife 4, e07090 (2015).
- [11] T. Nishimura, H. Honda, and M. Takeichi, *Planar Cell Polarity Links Axes of Spatial Dynamics in Neural-Tube Closure*, Cell 149, 1084 (2012).
- [12] E. Rozbicki, M. Chuai, A. I. Karjalainen, F. Song, H. M. Sang, R. Martin, H.-J. Knölker, M. P. MacDonald, and C. J. Weijer, Myosin-II-Mediated Cell Shape Changes and Cell Intercalation Contribute to Primitive Streak Formation, Nat. Cell Biol. 17, 397 (2015).
- [13] C. Bertet, L. Sulak, and T. Lecuit, *Myosin-Dependent Junction Remodelling Controls Planar Cell Intercalation and Axis Elongation*, Nature (London) **429**, 667 (2004).
- [14] K. E. Kasza, D. L. Farrell, and J. A. Zallen, Spatiotemporal Control of Epithelial Remodeling by Regulated Myosin Phosphorylation, Proc. Natl. Acad. Sci. U.S.A. 111, 11732 (2014).
- [15] E. Heller, K. V. Kumar, S. W. Grill, and E. Fuchs, Forces Generated by Cell Intercalation Tow Epidermal Sheets in Mammalian Tissue Morphogenesis, Dev. Cell 28, 617 (2014).
- [16] S. Curran, C. Strandkvist, J. Bathmann, M. de Gennes, A. Kabla, G. Salbreux, and B. Baum, *Myosin II Controls Junction Fluctuations to Guide Epithelial Tissue Ordering*, Dev. Cell 43, 480 (2017).
- [17] S. Nishio, X. Tian, A. R. Gallagher, Z. Yu, V. Patel, P. Igarashi, and S. Somlo, *Loss of Oriented Cell Division*

- *Does Not Initiate Cyst Formation*, Journal of the American Society of Nephrology: JASN **21**, 295 (2010).
- [18] D. S. Banerjee, A. Munjal, T. Lecuit, and M. Rao, Actomyosin Pulsation and Flows in an Active Elastomer with Turnover and Network Remodeling, Nat. Commun. 8, 1 (2017).
- [19] R. Fernandez-Gonzalez, S. de Matos Simoes, J.-C. Röper, S. Eaton, and J. A. Zallen, *Myosin II Dynamics Are Regulated by Tension in Intercalating Cells*, Dev. Cell 17, 736 (2009).
- [20] A. Munjal, J.-M. Philippe, E. Munro, and T. Lecuit, A Self-Organized Biomechanical Network Drives Shape Changes during Tissue Morphogenesis, Nature (London) 524, 351 (2015).
- [21] M. Rauzi, P.-F. Lenne, and T. Lecuit, *Planar Polarized Actomyosin Contractile Flows Control Epithelial Junction Remodelling*, Nature (London) **468**, 1110 (2010).
- [22] T. E. Vanderleest, C. M. Smits, Y. Xie, C. E. Jewett, J. T. Blankenship, and D. Loerke, Vertex Sliding Drives Intercalation by Radial Coupling of Adhesion and Actomyosin Networks during Drosophila Germband Extension, eLife 7, e34586 (2018).
- [23] R. J. Tetley, G. B. Blanchard, A. G. Fletcher, R. J. Adams, and B. Sanson, Unipolar Distributions of Junctional Myosin II Identify Cell Stripe Boundaries That Drive Cell Intercalation throughout Drosophila Axis Extension, eLife 5, e12094 (2016).
- [24] T. M. Finegan, N. Hervieux, A. Nestor-Bergmann, A. G. Fletcher, G. B. Blanchard, and B. Sanson, *The Tricellular Vertex-Specific Adhesion Molecule Sidekick Facilitates Polarised Cell Intercalation during Drosophila Axis Extension*, PLoS Biol. 17, 1 (2019).
- [25] R. J. Huebner, A. N. Malmi-Kakkada, S. Sarikaya, S. Weng, D. Thirumalai, and J. B. Wallingford, Cadherin Clustering Controls Heterogeneous, Asymmetric Junction Dynamics during Vertebrate Axis Elongation, eLife 10, e65390 (2021).
- [26] H. H. Yu and J. A. Zallen, *Abl and Canoe/Afadin Mediate Mechanotransduction at Tricellular Junctions*, Science **370**, eaba5528 (2020).
- [27] J. T. Blankenship, S. T. Backovic, J. S. P. Sanny, O. Weitz, and J. A. Zallen, *Multicellular Rosette Formation Links Planar Cell Polarity to Tissue Morphogenesis*, Dev. Cell 11, 459 (2006).
- [28] S. de Matos Simões, A. Mainieri, and J. A. Zallen, *Rho gtpase and shroom Direct Planar Polarized Actomyosin Contractility during Convergent Extension*, J. Cell Biol. **204**, 575 (2014).
- [29] X. Wang, M. Merkel, L. B. Sutter, G. Erdemci-Tandogan, M. L. Manning, and K. E. Kasza, *Anisotropy Links Cell Shapes to Tissue Flow during Convergent Extension*, Proc. Natl. Acad. Sci. U.S.A. 117, 13541 (2020).
- [30] K. V. Iyer, R. Piscitello-Gómez, J. Paijmans, F. Jülicher, and S. Eaton, *Epithelial Viscoelasticity Is Regulated by Mechanosensitive e-cadherin Turnover*, Curr. Biol. 29, 578 (2019).
- [31] R. J. Tetley and Y. Mao, *The Same but Different: Cell Intercalation as a Driver of Tissue Deformation and Fluidity*, Phil. Trans. R. Soc. B **373**, 20170328 (2018).

- [32] M. Takeichi, Dynamic Contacts: Rearranging Adherens Junctions to Drive Epithelial Remodelling, Nat. Rev. Mol. Cell Biol. 15, 397 (2014).
- [33] E. Scarpa and R. Mayor, Collective Cell Migration in Development, J. Cell Biol. 212, 143 (2016).
- [34] D. Cai, S.-C. Chen, M. Prasad, L. He, X. Wang, V. Choesmel-Cadamuro, J. K. Sawyer, G. Danuser, and D. J. Montell, Mechanical Feedback through e-cadherin Promotes Direction Sensing during Collective Cell Migration, Cell 157, 1146 (2014).
- [35] D. D. Shaye, J. Casanova, and M. Llimargas, Modulation of Intracellular Trafficking Regulates Cell Intercalation in the Drosophila Trachea, Nat. Cell Biol. 10, 964 (2008).
- [36] C. Revenu, S. Streichan, E. Donà, V. Lecaudey, L. Hufnagel, and D. Gilmour, Quantitative Cell Polarity Imaging Defines Leader-to-Follower Transitions during Collective Migration and the Key Role of Microtubule-Dependent Adherens Junction Formation, Development 141, 1282 (2014).
- [37] J.-A. Park et al., Unjamming and Cell Shape in the Asthmatic Airway Epithelium, Nat. Mater. 14, 1040 (2015), 26237129.
- [38] J. A. Mitchel, A. Das, M. J. O'Sullivan, I. T. Stancil, S. J. DeCamp, S. Koehler, O. H. Ocaña, J. P. Butler, J. J. Fredberg, M. A. Nieto et al., In Primary Airway Epithelial Cells, the Unjamming Transition Is Distinct from the Epithelial-to-Mesenchymal Transition, Nat. Commun. 11, 5053 (2020).
- [39] E. T. Roussos, M. Balsamo, S. K. Alford, J. B. Wyckoff, B. Gligorijevic, Y. Wang, M. Pozzuto, R. Stobezki, S. Goswami, J. E. Segall et al., Mena Invasive (menainv) Promotes Multicellular Streaming Motility and Transendothelial Migration in a Mouse Model of Breast Cancer, J. Cell Sci. 124, 2120 (2011).
- [40] P. Friedl, J.Locker, E. Sahai, and J. E. Segall, *Classifying Collective Cancer Cell Invasion*, Nat. Cell Biol. **14**, 777 (2012).
- [41] A. Patsialou, J. J. Bravo-Cordero, Y. Wang, D. Entenberg, H. Liu, M. Clarke, and J. S. Condeelis, *Intravital Multiphoton Imaging Reveals Multicellular Streaming as a Crucial Component of In Vivo Cell Migration in Human Breast Tumors*, Intravital **2**, e25294 (2013).
- [42] L. Oswald, S. Grosser, D. M. Smith, and J. A. Käs, Jamming Transitions in Cancer, J. Phys. D **50**, 483001 (2017).
- [43] O. Ilina, P. G. Gritsenko, S. Syga, J. Lippoldt, C. A. M. La Porta, O. Chepizhko, S. Grosser, M. Vullings, G.-J. Bakker, J. Starruß, P. Bult, S. Zapperi, J. A. Käs, A. Deutsch, and P. Friedl, Cell-Cell Adhesion and 3D Matrix Confinement Determine Jamming Transitions in Breast Cancer Invasion, Nat. Cell Biol. 22, 1103 (2020).
- [44] A. Comba, S. Motsch, P. J. Dunn, T. C. Hollon, D. B. Zamler, A. E. Argento, C. G. Kleer, M. G. Castro, and P. R. Lowenstein, Oncostreams: Self-Organization and Dynamics Determine Spatial Heterogeneity and Malignant Behavior in Gliomas, bioRxiv, https://doi.org/10.1101/2020.12.01.404970.
- [45] C. Malinverno, S. Corallino, F. Giavazzi, M. Bergert, Q. Li, M. Leoni, A. Disanza, E. Frittoli, A. Oldani, E. Martini

- et al., Endocytic Reawakening of Motility in Jammed Epithelia, Nat. Mater. 16, 587 (2017).
- [46] B. Slater, E. Ng, and A. P. McGuigan, Local Cell Coordination Does Not Alter Individual Cell Migration during Collective Migration But Does Impact Cellular Exchange Events, Integr. Biol. 11, 163 (2019).
- [47] T. Nagai and H. Honda, A Dynamic Cell Model for the Formation of Epithelial Tissues, Philos. Mag. B 81, 699 (2001).
- [48] R. Farhadifar, J.-C. Röper, B. Aigouy, S. Eaton, and F. Jülicher, *The Influence of Cell Mechanics, Cell-Cell Interactions, and Proliferation on Epithelial Packing*, Curr. Biol. **17**, 2095 (2007).
- [49] A. G. Fletcher, M. Osterfield, R. E. Baker, and S. Y. Shvartsman, *Vertex Models of Epithelial Morphogenesis*, Biophys. J. **106**, 2291 (2014).
- [50] P. Spahn and R. Reuter, A Vertex Model of Drosophila Ventral Furrow Formation, PLoS One 8, e75051 (2013).
- [51] M. F. Staddon, D. Bi, A. P. Tabatabai, V. Ajeti, M. P. Murrell, and S. Banerjee, Cooperation of Dual Modes of Cell Motility Promotes Epithelial Stress Relaxation to Accelerate Wound Healing, PLoS Comput. Biol. 14, e1006502 (2018).
- [52] M. A. Spencer, Z. Jabeen, and D. K. Lubensky, *Vertex Stability and Topological Transitions in Vertex Models of Foams and Epithelia*, Eur. Phys. J. E **40**, 2 (2017).
- [53] D. Bi, X. Yang, M. C. Marchetti, and M. L. Manning, *Motility-Driven Glass and Jamming Transitions in Biological Tissues*, Phys. Rev. X 6, 021011 (2016).
- [54] G. W. Brodland, Computational Modeling of Cell Sorting, Tissue Engulfment, and Related Phenomena: A Review, Appl. Mech. Rev. 57, 47 (2004).
- [55] M. Krajnc, S. Dasgupta, P. Ziherl, and J. Prost, *Fluidization of Epithelial Sheets by Active Cell Rearrangements*, Phys. Rev. E **98**, 022409 (2018).
- [56] D. Bi, J. H. Lopez, J. M. Schwarz, and M. L. Manning, A Density-Independent Rigidity Transition in Biological Tissues, Nat. Phys. 11, 1074 (2015).
- [57] L. Yan and D. Bi, *Multicellular Rosettes Drive Fluid-Solid Transition in Epithelial Tissues*, Phys. Rev. X **9**, 011029 (2019).
- [58] X. Li, A. Das, and D. Bi, *Mechanical Heterogeneity in Tissues Promotes Rigidity and Controls Cellular Invasion*, Phys. Rev. Lett. **123**, 058101 (2019).
- [59] X. Yang, D. Bi, M. Czajkowski, M. Merkel, M. L. Manning, and M. C.Marchetti, *Correlating Cell Shape and Cellular Stress in Motile Confluent Tissues*, Proc. Natl. Acad. Sci. U.S.A. 114, 12663 (2017).
- [60] F. Giavazzi, M. Paoluzzi, M. Macchi, D. Bi, G. Scita, M. L. Manning, R. Cerbino, and M. C. Marchetti, *Flocking Transitions in Confluent Tissues*, Soft Matter 14, 3471 (2018).
- [61] D. B. Staple, R. Farhadifar, J. C. Röper, B. Aigouy, S. Eaton, and F. Jülicher, *Mechanics and Remodelling of Cell Packings in Epithelia*, Eur. Phys. J. E 33, 117 (2010).
- [62] D. Bi, J. H. Lopez, J. M. Schwarz, and M. L. Manning, Energy Barriers and Cell Migration in Densely Packed Tissues, Soft Matter 10, 1885 (2014).
- [63] G.Erdemci-Tandogan and M. L. Manning, Effect of Cellular Rearrangement Time Delays on the Rheology of

- Vertex Models for Confluent Tissues, PLoS Comput. Biol. 17, e1009049 (2021).
- [64] M. D. Ediger, C. A. Angell, and S. R. Nagel, *Supercooled Liquids and Glasses*, J. Phys. Chem. **100**, 13200 (1996).
- [65] C. A. Angell, Formation of Glasses from Liquids and Biopolymers, Science 267, 1924 (1995).
- [66] A. van Blaaderen and P. Wiltzius, Real-Space Structure of Colloidal Hard-Sphere Glasses, Science 270, 1177 (1995).
- [67] E. R. Weeks, J. C. Crocker, A. C. Levitt, A. Schofield, and D. A. Weitz, *Three-Dimensional Direct Imaging of Structural Relaxation near the Colloidal Glass Transition*, Science 287, 627 (2000).
- [68] S. Karmakar, C. Dasgupta, and S. Sastry, Short-Time Beta Relaxation in Glass-Forming Liquids Is Cooperative in Nature, Phys. Rev. Lett. 116, 085701 (2016).
- [69] L. Berthier and G. Biroli, Theoretical Perspective on the Glass Transition and Amorphous Materials, Rev. Mod. Phys. 83, 587 (2011).
- [70] A. Fierro, E. Del Gado, A. de Candia, and A. Coniglio, Dynamical Heterogeneities in Attractive Colloids, J. Stat. Mech. (2008) L04002.
- [71] T. Abete, A. de Candia, E. Del Gado, A. Fierro, and A. Coniglio, *Static and Dynamic Heterogeneities in a Model for Irreversible Gelation*, Phys. Rev. Lett. 98, 088301 (2007).
- [72] R. Böhmer, K. L. Ngai, C. A. Angell, and D. J. Plazek, Nonexponential Relaxations in Strong and Fragile Glass Formers, J. Chem. Phys. 99, 4201 (1993).
- [73] A. Szabó, R. Ünnep, E. Méhes, W. O. Twal, W. S. Argraves, Y. Cao, and A. Czirók, *Collective Cell Motion in Endothelial Monolayers*, Phys. Biol. 7, 046007 (2010).
- [74] A. Hallou, J. Jennings, and A. J. Kabla, *Tumour Heterogeneity Promotes Collective Invasion and Cancer Metastatic Dissemination*, R. Soc. Open Sci. 4, 161007 (2017).
- [75] T. Das, K. Safferling, S. Rausch, N. Grabe, H. Boehm, and J. P. Spatz, *A Molecular Mechanotransduction Pathway Regulates Collective Migration of Epithelial Cells*, Nat. Cell Biol. **17**, 276 (2015).
- [76] A. J. Loza, S. Koride, G. V. Schimizzi, B. Li, S. X. Sun, and G. D. Longmore, Cell Density and Actomyosin Contractility Control the Organization of Migrating Collectives within an Epithelium, Mol. Biol. Cell 27, 3459 (2016), pMID: 27605707.
- [77] P. Friedl and R. Mayor, *Tuning Collective Cell Migration* by Cell–Cell Junction Regulation, Cold Spring Harbor Perspect. Biol. **9**, a029199 (2017).
- [78] A. Czirók, K. Varga, E. Méhes, and A. Szabó, Collective Cell Streams in Epithelial Monolayers Depend on Cell Adhesion, New J. Phys. 15, 075006 (2013).
- [79] A. N. Malmi-Kakkada, X. Li, H. S. Samanta, S. Sinha, and D. Thirumalai, Cell Growth Rate Dictates the Onset of Glass to Fluidlike Transition and Long Time Superdiffusion in an Evolving Cell Colony, Phys. Rev. X 8, 021025 (2018).
- [80] D. A. Matoz-Fernandez, K. Martens, R. Sknepnek, J. L. Barrat, and S. Henkes, *Cell Division and Death Inhibit Glassy Behaviour of Confluent Tissues*, Soft Matter 13, 3205 (2017).

- [81] M. Czajkowski, D. M. Sussman, M. C. Marchetti, and M. L. Manning, Glassy Dynamics in Models of Confluent Tissue with Mitosis and Apoptosis, Soft Matter 15, 9133 (2019).
- [82] J. Devany, D. M. Sussman, T. Yamamoto, M. L. Manning, and M. L. Gardel, *Cell Cycle-Dependent Active Stress Drives Epithelia Remodeling*, Proc. Natl. Acad. Sci. U.S.A. 118, e1917853118 (2021).
- [83] S. Henkes, Y. Fily, and M. C. Marchetti, *Active Jamming: Self-Propelled Soft Particles at High Density*, Phys. Rev. E 84, 040301(R) (2011).
- [84] R. Mandal, P. J. Bhuyan, P. Chaudhuri, M. Rao, and C. Dasgupta, *Glassy Swirls of Active Dumbbells*, Phys. Rev. E 96, 042605 (2017).
- [85] R. Mandal, P. J. Bhuyan, P. Chaudhuri, C. Dasgupta, and M. Rao, Extreme Active Matter at High Densities, Nat. Commun. 11, 2581 (2020).
- [86] S. Henkes, K. Kostanjevec, J. M. Collinson, R. Sknepnek, and E. Bertin, *Dense Active Matter Model of Motion Patterns in Confluent Cell Monolayers*, Nat. Commun. 11, 1405 (2020).
- [87] A. D. S. Parmar and S. Sastry, *Kinetic and Thermodynamic Fragilities of Square Well Fluids with Tunable Barriers to Bond Breaking*, J. Phys. Chem. B **119**, 11243 (2015), pMID: 26134744.
- [88] J.-L. Barrat and L. Berthier, Fluctuation-Dissipation Relation in a Sheared Fluid, Phys. Rev. E 63, 012503 (2000).
- [89] A. Furukawa, K. Kim, S. Saito, and H.Tanaka, *Anisotropic Cooperative Structural Rearrangements in Sheared Supercooled Liquids*, Phys. Rev. Lett. **102**, 016001 (2009).
- [90] H. Mizuno and R. Yamamoto, Dynamical Heterogeneity in a Highly Supercooled Liquid under a Sheared Situation, J. Chem. Phys. 136, 084505 (2012).
- [91] T. S. Ingebrigtsen and H. Tanaka, Structural Predictor for Nonlinear Sheared Dynamics in Simple Glass-Forming Liquids, Proc. Natl. Acad. Sci. U.S.A. 115, 87 (2018).
- [92] A. Ikeda, L. Berthier, and P. Sollich, *Unified Study of Glass and Jamming Rheology in Soft Particle Systems*, Phys. Rev. Lett. **109**, 018301 (2012).
- [93] C. Donati, J. F. Douglas, W. Kob, S. J. Plimpton, P. H. Poole, and S. C. Glotzer, *Stringlike Cooperative Motion in a Supercooled Liquid*, Phys. Rev. Lett. **80**, 2338 (1998).
- [94] S. Koride, A. J. Loza, and S. X. Sun, Epithelial Vertex Models with Active Biochemical Regulation of Contractility Can Explain Organized Collective Cell Motility, APL Bioeng. 2, 031906 (2018).

- [95] S. Toda, L. R. Blauch, S. K. Y. Tang, L. Morsut, and W. A. Lim, Programming Self-Organizing Multicellular Structures with Synthetic Cell-Cell Signaling, Science 361, 156 (2018).
- [96] P. Q. Nguyen, N.-M. D. Courchesne, A. Duraj-Thatte, P. Praveschotinunt, and N. S. Joshi, Engineered Living Materials: Prospects and Challenges for Using Biological Systems to Direct the Assembly of Smart Materials, Adv. Mater. 30, 1704847 (2018).
- [97] M. Xie and M. Fussenegger, Designing Cell Function: Assembly of Synthetic Gene Circuits for Cell Biology Applications, Nat. Rev. Mol. Cell Biol. 19, 507 (2018).
- [98] B. P. Teague, P. Guye, and R. Weiss, Synthetic Morphogenesis, Cold Spring Harbor Perspect. Biol. 8, a023929 (2016).
- [99] S. Okuda, Y. Inoue, M. Eiraku, T. Adachi, and Y. Sasai, Vertex Dynamics Simulations of Viscosity-Dependent Deformation during Tissue Morphogenesis, Biomech. Model. Mechanobiol. 14, 413 (2015).
- [100] C. Bechinger, R. Di Leonardo, H. Löwen, C. Reichhardt, G. Volpe, and G. Volpe, *Active Particles in Complex and Crowded Environments*, Rev. Mod. Phys. 88, 045006 (2016).
- [101] M. E. Cates and J. Tailleur, Motility-Induced Phase Separation, Annu. Rev. Condens. Matter Phys. 6, 219 (2015).
- [102] Y. Fily, S. Henkes, and M. C. Marchetti, Freezing and Phase Separation of Self-Propelled Disks, Soft Matter 10, 2132 (2014).
- [103] Y. Fily and M. C. Marchetti, *Athermal Phase Separation of Self-Propelled Particles with No Alignment*, Phys. Rev. Lett. **108**, 235702 (2012).
- [104] H. Chaté, F. Ginelli, G. Grégoire, and F. Raynaud, Collective Motion of Self-Propelled Particles Interacting without Cohesion, Phys. Rev. E 77, 046113 (2008).
- [105] K. A. Brakke, The Surface Evolver, Exp. Math. 1, 141 (1992).
- [106] R. S. L. Stein and H. C. Andersen, Scaling Analysis of Dynamic Heterogeneity in a Supercooled Lennard-Jones Liquid, Phys. Rev. Lett. 101, 267802 (2008).
- [107] D. M. Sussman, M. Paoluzzi, M. C. Marchetti, and M. L. Manning, Anomalous Glassy Dynamics in Simple Models of Dense Biological Tissue, Europhys. Lett. 121, 36001 (2018)
- [108] W. Kob, C. Donati, S. J. Plimpton, P. H. Poole, and S. C. Glotzer, *Dynamical Heterogeneities in a Supercooled Lennard-Jones Liquid*, Phys. Rev. Lett. **79**, 2827 (1997).